J. Fluid Mech. (1999), *vol.* 401, *pp.* 123–156. Printed in the United Kingdom

Suboptimal feedback control of vortex shedding at low Reynolds numbers

By CHULHONG MIN AND HAECHEON CHOI†

School of Mechanical and Aerospace Engineering, Seoul National University, Seoul 151-742, Korea

(Received 19 February 1998 and in revised form 24 June 1999)

The objective of this study is to develop a method of controlling vortex shedding behind a bluff body using control theory. A suboptimal feedback control procedure for local sensing and local actuation is developed and applied to the flow behind a circular cylinder. The location of sensors for feedback is limited to the cylinder surface and the control input from actuators is the blowing and suction on the cylinder surface. Three different cost functionals to be minimized (J_1 and J_2) or maximized (J_3) are investigated: J_1 is proportional to the pressure drag of the cylinder, J_2 is the square of the difference between the target pressure (inviscid flow pressure) and real flow pressure on the cylinder surface, and J_3 is the square of the pressure gradient on the cylinder surface, respectively. Given the cost functionals, the flow variable to be measured by the sensors and the control input from the actuators are determined from the suboptimal feedback control procedure. Several cases for each cost functional have been numerically simulated at $Re = 100$ and 160 to investigate the performance of the control algorithm. For all actuations, vortex shedding becomes weak or disappears, and the mean drag and drag/lift fluctuations significantly decrease. For a given magnitude of the blowing/suction, reducing J_2 provides the largest drag reduction among the three cost functionals.

1. Introduction

The phenomenon of vortex shedding behind a circular cylinder has been a major topic of fluid mechanics research (Williamson 1996). Since Roshko (1955) measured the vortex shedding period behind a bluff body, many researchers have investigated vortex shedding behind a circular cylinder at low Reynolds numbers. When vortex shedding appears, mean drag and fluctuations of drag and lift increase. Furthermore, drag and lift fluctuations shorten the life of a structure. On the other hand, vortex shedding enhances mixing behind a circular cylinder. Therefore, controlling vortex shedding is very important in practical situations and many researchers have been investigating various control methods to passively or actively control it and thus to reduce mean drag and drag/lift fluctuations, or to enhance mixing.

There have been many passive or non-feedback active ways of controlling vortex shedding: for example, endplates (Nishioka & Sato 1974; Stansby 1974), inhomogeneous inlet flows (Gaster 1969, 1971; Gerich & Eckelmann 1982), splitter plates (Roshko 1955; Gerrard 1966; Apelt, West & Szewczyk 1973; Apelt & West 1975;

† Corresponding author: e-mail: choi@socrates.snu.ac.kr. Also at the National CRI Center for Turbulence and Flow Control Research, Institute of Advanced Machinery and Design, Seoul National University.

Unal & Rockwell 1988; Cimbala & Garg 1991; Kwon & Choi 1996), blockage (Shair *et al.* 1963), a second cylinder in the wake (Strykowski & Sreenivasan 1990), base bleed (Wood 1964; Bearman 1967; Schumm, Berger & Monkewitz 1994), and periodic rotation of the cylinder (Tokumaru & Dimotakis 1991). These control methods are passive or non-feedback active in the sense that there is no energy input or no feedback sensor, respectively.

Recently, a few active and feedback ways of controlling vortex shedding have been investigated. Roussopoulos (1993) conducted feedback control using a speaker based on the velocity phase information measured at a point in the wake. As a result, complete suppression of vortex shedding was possible up to 10 units of the Reynolds number above the onset of shedding. A similar feedback approach was conducted by Park, Ladd & Hendricks (1994) using a pair of blowing/suction slots on the cylinder and a single feedback sensor located in the wake. They showed a complete suppression of vortex shedding at $Re = 60$.

Most of those control methods, however, are based on physical intuition through observation of flow phenomena. When flow phenomena are too complex to understand, it is not an easy task to develop a control scheme based on physical intuition, and thus one may have to rely on more systematic control methods. Theoretically oriented work on controlling fluid flow can be found in Abergel & Temam (1990) and in a series of articles by Gunzburger, Hou & Svobodny (1990, 1991, 1992). Abergel & Temam (1990) applied an optimal control theory to some fluid mechanics problems and derived optimality conditions for various physical situations, but the application of their optimal control algorithm to the unsteady three-dimensional Navier–Stokes equations is not practical owing to the great complexity of the algorithm. Gunzburger *et al.* (1990, 1991, 1992) also considered various optimal control problems in fluid mechanics and studied mathematical and numerical problems such as the existence of optimal controls, necessary optimality conditions of the first order, the discretization of those problems by finite element, and convergence and error estimates for the discrete problems. Recently, Temam, Bewley & Moin (1997) applied an optimal feedback control procedure to a low-Reynolds-number turbulent channel flow and reported a significant amount of drag reduction and, in some cases, relaminarization of the turbulent flow. The procedure developed by them, however, still required velocity information inside the flow in order to solve the adjoint equations, from which a feedback control input was derived.

In order to overcome the complexity of the procedure developed by Abergel & Temam (1990), Choi *et al.* (1993*b*) introduced a suboptimal feedback control algorithm, in which the iterations required for a global optimal control were avoided by seeking an optimal condition over a short time period. The suboptimal control procedure was successfully applied to control of the stochastic Burgers equation. Satake & Kasagi (1997) applied unsteady momentum forcing, obtained from the suboptimal control procedure, to a turbulent channel flow and showed that a significant amount of drag reduction is achieved by controlling near-wall spanwise velocity fluctuations, but their approach needed velocity information near the wall. Recently, Lee, Kim & Choi (1998) applied unsteady blowing and suction to a turbulent channel flow and reported that the suboptimal feedback control procedure using pressure or shear-stress information only at the wall resulted in 16%–22% reduction of the skin-friction drag.

In the previous studies on feedback control of vortex shedding behind a circular cylinder at low Reynolds numbers (Roussopoulos 1993; Park *et al.* 1994), feedback sensors were located in the wake and feedback controllers were constructed based on physical intuition through observation of flow phenomena. Their control purpose

was to stabilize the wake instability. In the present study, our control purpose is different from the previous one in the sense that we develop a *systematic* control method using the suboptimal feedback control scheme, which may be applied to both laminar and turbulent flows, in order to achieve drag reduction through control of vortex shedding behind a circular cylinder. Also, we restrict the location of feedback sensors to the cylinder surface because implementation of the sensor in the wake is not practical in many real situations. The control input from actuators is the blowing and suction on the cylinder surface. We will show that vortex shedding can be successfully controlled using information only on the cylinder surface and drag is reduced accordingly. Governing equations and numerical details are described in § 2. In § 3, cost functionals expected to reduce drag of the circular cylinder are defined, and a suboptimal feedback control procedure for each cost functional is presented in § 4. Results are shown in § 5, followed by a summary in § 6. Detailed derivations of equations in § 4 are given in Appendices A and B.

2. Governing equations and numerical details

In this study, we numerically simulate the incompressible Navier–Stokes and continuity equations

$$\frac{\partial u_i}{\partial t} + \frac{\partial u_i u_j}{\partial x_j} = -\frac{\partial p}{\partial x_i} + \frac{1}{Re}\frac{\partial^2 u_i}{\partial x_j \partial x_j}, \tag{2.1}$$

$$\frac{\partial u_i}{\partial x_i} = 0, \tag{2.2}$$

where t is time, x_i are the coordinates, u_i are the velocity components, p is the pressure and $Re = u_\infty d/\nu$ is the Reynolds number. Here u_∞ is the free-stream velocity, d the diameter, and ν the kinematic viscosity.

Rewriting (2.1) and (2.2) in a generalized coordinate system (η_1, η_2) yields

$$\frac{\partial Q_i}{\partial t} + H_i = -P_i + \frac{1}{Re} D_i, \tag{2.3}$$

$$\frac{\partial Q_i}{\partial \eta_i} = 0, \tag{2.4}$$

with

$$Q_i = \zeta_j^i u_j, \tag{2.5}$$

$$c_j^i = \frac{\partial x_i}{\partial \eta_j}, \tag{2.6}$$

$$\zeta_j^i = \mathscr{J}(c_i^j)^{-1}, \tag{2.7}$$

$$\mathscr{J} = \sqrt{||c_i^k c_j^k||}, \tag{2.8}$$

where $i, j, k = 1, 2$, H_i are the nonlinear terms, P_i are the pressure terms, D_i are the diffusion terms, and Q_i are the volume fluxes across the faces of the cells, which are equivalent to using the contravariant velocity components on a staggered grid multiplied by the Jacobian ($\mathscr{J}$) of the coordinate transformation. Using this choice, discretized mass conservation can be easily satisfied (Rosenfeld, Kwak & Vinokur 1991; Choi, Moin & Kim 1992, 1993*a*). For details, refer to Choi *et al.* (1992).

To solve (2.3) and (2.4), a fully implicit (Crank–Nicolson) fractional step method

is used in time and a second-order central difference method is used in space with a staggered grid. A multigrid method and a Newton-iterative method are used to solve the Poisson equation and the discretized nonlinear momentum equations, respectively. This scheme has been successfully applied to a turbulent flow over riblets (Choi *et al.* 1993*a*) and a laminar flow past a circular cylinder (Kwon & Choi 1996).

Figure 1 shows the grid system, flow geometry and coordinate system along with boundary conditions. A C-type grid system is known for better resolution in the wake region than an O-type grid system (Thompson, Warsi & Mastin 1985). The computational domain used is $-50d < x < 20d$ and $-50d < y < 50d$, where $x = 0$ and $y = 0$ corresponds to the centre location of the cylinder in the Cartesian coordinate system. A non-uniform mesh of 321×121 points is created using a hyperbolic grid generation technique and 64 grid points are located on the cylinder surface.

A periodic boundary condition is used at the branch cut and a convective outflow condition, $\partial u_i/\partial t + c\partial u_i/\partial x = 0$, is used for the outflow boundary condition (Pauley, Moin & Reynolds 1990), where c is the space-averaged streamwise velocity at the exit. This boundary condition allows vortices to smoothly pass away out of computational domain. Dirichlet boundary conditions are used at far-field boundaries and also at the cylinder surface.

The current mesh and domain size have been determined from an extensive study of the numerical parameters (e.g. computational domain size, number of grid points, skewness of the computational mesh, etc.). We have found from this study that the domain size in the y-direction is more critical in accurately predicting the Strouhal number than the domain size in the streamwise (x) direction. The predicted Strouhal numbers at $50 \leqslant Re \leqslant 160$ were in excellent agreement with those obtained by Williamson (1989) and Henderson (1997) (see also Kwon & Choi 1996). Doubling the domain size and grid points in both directions changed the predicted Strouhal number by less than 0.5%.

For all cases investigated in this study, we have used a computational time step, $\Delta t = 0.015$, which corresponds to CFL ≈ 1. About two Newton iterations are needed to solve the discretized nonlinear momentum equations. We have also simulated the flow with half the time step, which resulted in only 0.1% change of the predicted drag coefficient. The CPU time required is about 3.5 CRAY YMP C90 seconds per time step.

3. Problem setting

The phenomenon of vortex shedding behind a circular cylinder at low Reynolds numbers is very interesting. At a very low Reynolds number ($Re \ll 1$), flow around a circular cylinder is steady and symmetric upstream and downstream. As the Reynolds number increases, the upstream–downstream symmetry disappears and two attached eddies appear behind a cylinder. These eddies grow bigger with increasing Reynolds number. For $Re \gtrsim 47$, unsteadiness arises spontaneously even though all the imposed conditions are being held steady and vortex shedding appears behind the circular cylinder, resulting in the increase of the pressure drag. In two-dimensional flow, as Re increases, drag of a circular cylinder increases (Tritton 1987; Henderson 1995).

Fornberg (1980) simulated the flow past a circular cylinder using a steady code and obtained the drag coefficient of $C_d = 1.058$ at $Re = 100$. In experiments, however, C_d varies from 1.26 to 1.40 at $Re = 100$ (Oertel 1990; Panton 1996) which is much larger than the numerical simulation result of Fornberg. This difference is mainly due to the existence of vortex shedding behind a circular cylinder which cannot be simulated

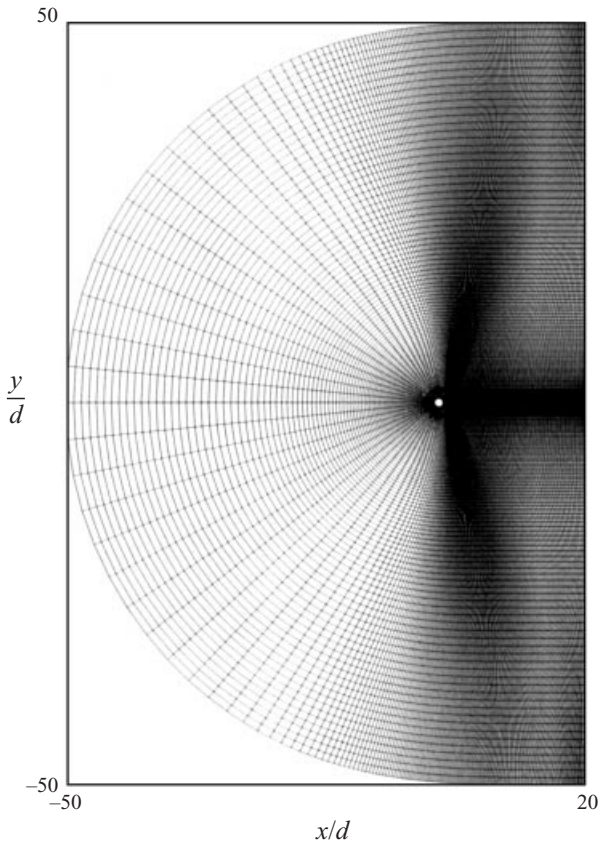

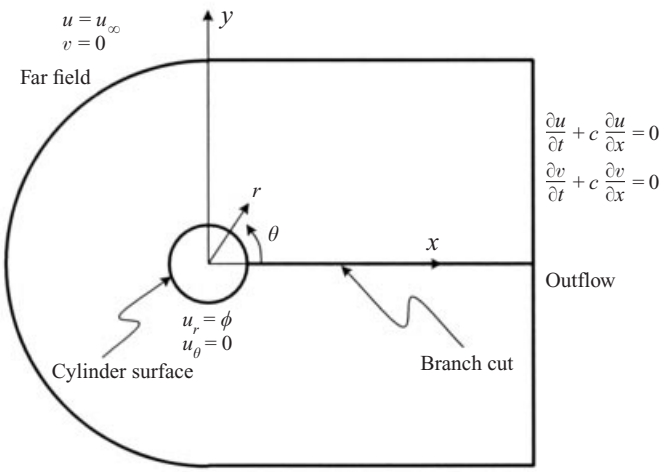

FIGURE 1. Grid system, flow geometry and coordinate system along with boundary conditions.

correctly by the steady solution. Recently, there have been many numerical studies on flow behind a circular cylinder using an unsteady Navier–Stokes code and they accurately predicted vortex shedding (see, for example, Park *et al.* 1994; Henderson 1995; Kwon & Choi 1996; Henderson 1997). Henderson (1995) and Kwon & Choi

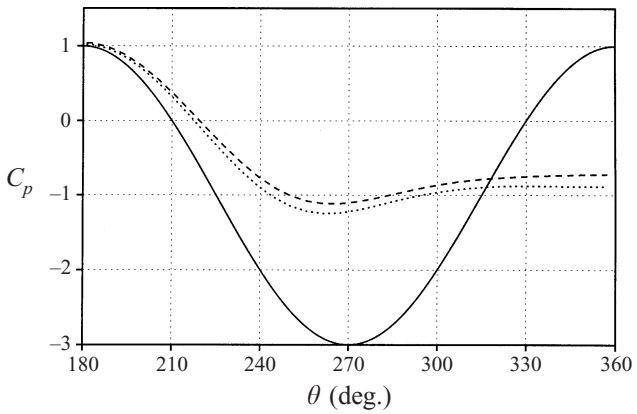

FIGURE 2. Time-averaged pressure coefficients on the cylinder surface: ———, inviscid flow (p_t); – – – –, $Re = 100$; ·····, $Re = 160$. Here, $\theta = 180°$ and $360°$ correspond to the stagnation and base points, respectively.

(1996) obtained the drag coefficients of 1.35 and 1.337 at $Re = 100$, respectively, which are closer to the result of experiments. From these results, it is clear that there is a close relation between vortex shedding and the drag of a circular cylinder.

We, therefore, define three cost functionals to control vortex shedding which would be expected to reduce the drag of a circular cylinder. These cost functionals are functions of the actuation ϕ (blowing/suction on the cylinder surface in the present study)

$$J_1(\phi) = \int -p(\theta)|_{r=R} \cos\theta R \, \mathrm{d}\theta, \tag{3.1}$$

$$J_2(\phi) = \frac{1}{2} \int \left(p_t - p(\theta)|_{r=R}\right)^2 R \, \mathrm{d}\theta, \tag{3.2}$$

$$J_3(\phi) = \frac{1}{2} \int \left(\frac{\partial p(\theta)}{\partial \theta}\bigg|_{r=R} \right)^2 R \, \mathrm{d}\theta, \tag{3.3}$$

where R is the cylinder radius, $p(\theta)|_{r=R}$ is the pressure on the cylinder surface and p_t is a target pressure on the cylinder surface.

J_1 is the *instantaneous* pressure drag of a circular cylinder, which increases due to vortex shedding, and thus decreasing J_1 directly reduces the pressure drag. One should, however, note that total drag is composed of the pressure drag and the skin-friction drag. Reducing the pressure drag, therefore, does not guarantee reduction of total drag. One may also consider a cost functional defined as $J(\phi) = (1/T) \int_0^T \int -p(\theta)|_{r=R} \cos\theta R \, \mathrm{d}\theta \, \mathrm{d}t$. This cost functional is associated with optimal control (rather than suboptimal control). The optimal control approach of minimizing or maximizing the cost functional in a global time period requires the iterative solutions of the Navier–Stokes equations and their adjoint on the whole and large interval (0, T) as well as the storage of the velocity and adjoint velocity fields for the iterative solutions (see Abergel & Temam 1990). Such computations are out of reach at this time.

Second, J_2 is the square of the difference between the target pressure and the real pressure of a circular cylinder. In this study, we consider the inviscid flow pressure on the cylinder surface as the target pressure. Figure 2 shows the time-averaged

pressure distributions on the cylinder surface for inviscid flow and viscous flows at $Re = 100$ and 160, where $C_p = (p - p_\infty)/(\frac{1}{2}\rho u_\infty^2)$ is the time-averaged pressure coefficient, ρ is the density, and p_∞ and u_∞ are the free-stream pressure and free-stream velocity, respectively. From this figure, we can easily note that according to the inviscid theory, a circular cylinder has no drag and lift because there are no pressure difference between upstream and downstream and no shear force on the cylinder surface. Real viscous flow past a circular cylinder, however, has a pressure difference between upstream and downstream and also has a shear force on the cylinder surface, resulting in mean drag and drag/lift fluctuations. We can, therefore, easily predict that when the real pressure on the cylinder surface is forced to be the same as the inviscid flow pressure, there will be no pressure drag of the cylinder. Hence, decreasing J_2 is expected to reduce the drag of a circular cylinder. On the other hand, one may also define another unsteady flow as the desired low drag state. For example, for the control of vortex shedding at $Re = 160$, one could set up the target pressure on the cylinder surface as the pressure at $Re = 100$, because the drag at $Re = 100$ is smaller than that at $Re = 160$. Implementation of this kind of target pressure into the control procedure is straightforward and very similar to that shown in § 4.

Finally, J_3 is the square of the pressure gradient on the cylinder surface. From figure 2, we can see that the pressure gradient on the cylinder surface of the inviscid flow is much larger than that of real flow. Therefore, *increasing* J_3 is expected to reduce the drag of a circular cylinder. In transonic flow, however, increasing the pressure gradient on the cylinder surface does not necessarily decrease drag due to the existence of shock waves which significantly change the pressure distribution on the surface. This high-speed flow case is not considered in the present study.

Hence, decreasing J_1 and J_2 or increasing J_3 would be expected to control vortex shedding behind a circular cylinder and thus reduce drag.

4. Suboptimal feedback control procedure

4.1. *Fréchet differential states*

As mentioned in § 3, the cost functionals J_1, J_2 and J_3 are functions of the actuation ϕ, and, thus, to minimize or maximize the cost functionals, we need to find the Fréchet differential states of the velocity and pressure, (q_i, ρ), using the Fréchet differential (Finlayson 1972),

$$q_i = \frac{\mathscr{D}u_i^{n+1}}{\mathscr{D}\phi^{n+1}}\tilde{\phi}^{n+1}, \tag{4.1}$$

$$\rho = \frac{\mathscr{D}p^{n+1}}{\mathscr{D}\phi^{n+1}}\tilde{\phi}^{n+1}, \tag{4.2}$$

with

$$\frac{\mathscr{D}f(\phi)^{n+1}}{\mathscr{D}\phi^{n+1}}\tilde{\phi}^{n+1} = \lim_{\epsilon \to 0}\frac{f(\phi + \epsilon\tilde{\phi})^{n+1} - f(\phi)^{n+1}}{\epsilon}, \tag{4.3}$$

where $\tilde{\phi}$ is an arbitrary perturbation field to ϕ and the superscript $n+1$ denotes the control time step at which a new actuation is applied.

To find (q_i, ρ), we should solve the Fréchet differential equations which are derived from the Navier–Stokes and continuity equations with given boundary conditions. There are two ways to do this. One way is to solve the linearized adjoint Navier–Stokes equations with adjoint boundary conditions which are derived from the Fréchet differential equations and the cost functional (Choi *et al.* 1993*b*). The other way

is to directly solve the Fréchet differential equations with the use of the Fourier transformation (Lee *et al.* 1998). These two methods yield the same solutions of the Fréchet differential states. The latter method is more straightforward than the first, but it is restricted to very simple flow geometry problems such as channel or cylinder, owing to the Fourier transformation. In the present study, we use the latter method.

The problem under consideration is a two-dimensional circular cylinder flow, for which the governing equations are the incompressible Navier–Stokes and continuity equations with boundary conditions

$$\frac{\partial u_i}{\partial t} + \frac{\partial u_i u_j}{\partial x_j} = -\frac{\partial p}{\partial x_i} + \frac{1}{Re}\frac{\partial^2 u_i}{\partial x_j \partial x_j}, \tag{4.4}$$

$$\frac{\partial u_i}{\partial x_i} = 0, \tag{4.5}$$

with

$$\left.\begin{aligned} u_r|_{r=R} &= \phi, & u_\theta|_{r=R} &= 0, \\ u_r|_{r\to\infty} &= \cos\theta, & u_\theta|_{r\to\infty} &= -\sin\theta, \end{aligned}\right\} \tag{4.6}$$

where r and θ are the cylindrical coordinates, u_r and u_θ are the velocities in the (r, θ) directions, respectively, and ϕ is the control input which is the surface-normal velocity (blowing/suction) on the cylinder surface. All variables are non-dimensionalized by the free-stream velocity u_∞ and the cylinder diameter d.

Formulation of a suboptimal feedback control procedure depends on the numerical time discretization of the Navier–Stokes equations (Choi *et al.* 1993*b*). We choose the Crank–Nicolson scheme for the linear terms and a Runge–Kutta scheme for the nonlinear terms to yield a discretized form of (4.4)–(4.6)

$$u_i^{n+1} + \frac{\Delta t_c}{2}\frac{\partial p^{n+1}}{\partial x_i} - \frac{\Delta t_c}{2Re}\frac{\partial^2 u_i^{n+1}}{\partial x_j \partial x_j} = RHS^n, \tag{4.7}$$

$$\frac{\partial u_i^{n+1}}{\partial x_i} = 0, \tag{4.8}$$

with

$$\left.\begin{aligned} u_r|_{r=R}^{n+1} &= \phi^{n+1}, & u_\theta|_{r=R}^{n+1} &= 0, \\ u_r|_{r\to\infty}^{n+1} &= \cos\theta, & u_\theta|_{r\to\infty}^{n+1} &= -\sin\theta, \end{aligned}\right\} \tag{4.9}$$

where Δt_c is the control time interval (i.e. at every Δt_c the control input ϕ is updated) and RHS^n is the nonlinear term and the explicit parts of the pressure gradient and viscous terms at control time step n. In this way, the actuation values are determined from the pressure information only on the cylinder surface (see § 4.2). Neglecting the nonlinear terms in constructing a controller may miss important flow dynamics, but Lee *et al.* (1998) found from numerical tests with the full nonlinear terms included that the contribution from the nonlinear terms is negligible in the boundary control of turbulent channel flow with a short time interval Δt_c; it turns out that the conservation of mass due to the wall actuation dominates the near-wall dynamics.

Note that the time discretization method adopted for constructing the suboptimal feedback controller does not have to be the same as the time integration method for obtaining accurate flow fields in time, and should be determined from consideration of the practical implementation of the control algorithm (see Choi *et al.* 1993*b*). Note also that the control time interval Δt_c is not necessarily the same as the computational time step Δt (see § 5).

Next, the Fréchet differential of (4.7)–(4.9) yields the governing equations for the Fréchet differential states (q_i, ρ) with boundary conditions

$$q_i + \frac{\Delta t_c}{2}\frac{\partial \rho}{\partial x_i} - \frac{\Delta t_c}{2Re}\frac{\partial^2 q_i}{\partial x_j \partial x_j} = 0, \tag{4.10}$$

$$\frac{\partial q_i}{\partial x_i} = 0, \tag{4.11}$$

with

$$\left.\begin{aligned} q_r|_{r=R} &= \tilde{\phi}, \quad q_\theta|_{r=R} = 0, \\ q_r|_{r\to\infty} &= 0, \quad q_\theta|_{r\to\infty} = 0, \end{aligned}\right\} \tag{4.12}$$

where q_i and ρ are defined in (4.1) and (4.2). Note that $\mathscr{D}\{RHS^n\}/\mathscr{D}\phi^{n+1}\ \tilde{\phi}^{n+1} = 0$.

By taking the divergence of (4.10) and using (4.11), we get a Laplace equation for ρ,

$$\frac{\partial^2 \rho}{\partial x_i \partial x_i} = 0. \tag{4.13}$$

From (4.10)–(4.13), we obtain the following analytic solution of the Fréchet differential state equations using the Fourier transformation in the circumferential direction (see Appendix A):

$$\hat{q}_{r,k=0} = \frac{\hat{\tilde{\phi}}_{k=0}}{K_1(mR)} K_1(mr), \tag{4.14}$$

$$\hat{q}_{\theta,k=0} = 0, \tag{4.15}$$

$$\hat{\rho}_{k=0} = \hat{\rho}_{r=R,k=0} (= \text{constant}), \tag{4.16}$$

$$\hat{q}_{r,k\neq 0} = \hat{\tilde{\phi}}_{k\neq 0} \frac{A\left(R/r\right)^{|k|} + R|k|K_{|k|}(mr)}{B\ r}, \tag{4.17}$$

$$\hat{q}_{\theta,k\neq 0} = \frac{\mathrm{i}|k|}{k}\hat{\tilde{\phi}}_{k\neq 0} \frac{-A\left(R/r\right)^{|k|} + \left\{R|k|K_{|k|}(mr) - mRrK_{|k|+1}(mr)\right\}}{B\ r}, \tag{4.18}$$

$$\hat{\rho}_{k\neq 0} = \frac{2}{\Delta t_c}\frac{1}{|k|}\hat{\tilde{\phi}}_{k\neq 0}\frac{A}{B}\left(\frac{R}{r}\right)^{|k|}, \tag{4.19}$$

with

$$A = R|k|K_{|k|}(mR) - mR^2 K_{|k|+1}(mR), \tag{4.20}$$

$$B = 2|k|K_{|k|}(mR) - mRK_{|k|+1}(mR), \tag{4.21}$$

$$m = \sqrt{\frac{2Re}{\Delta t_c}}, \tag{4.22}$$

where k is the wavenumber in the circumferential direction, $\hat{q}_{r,k}$, $\hat{q}_{\theta,k}$, $\hat{\rho}_k$ and $\hat{\tilde{\phi}}_k$ are the Fourier coefficients of q_r, q_θ, ρ and $\tilde{\phi}$, respectively, and $K_{|k|}$ is the modified Bessel function of the second kind, of order $|k|$. Note that $\hat{\tilde{\phi}}_{k=0}$ and $\hat{\rho}_{r=R,k=0}$ are the mean values of $\tilde{\phi}$ and ρ on the cylinder surface, respectively. From the continuity ((4.8) and (4.11)) and boundary conditions specified in this study ((4.9) and (4.12)), it is clear that $\hat{\phi}_{k=0}$(mean value of ϕ) $= \hat{\tilde{\phi}}_{k=0} = 0$. It should be noted however that non-zero mean values of ϕ can be easily implemented in the suboptimal control

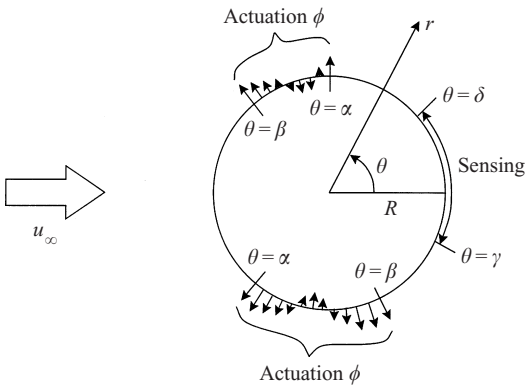

FIGURE 3. Schematic of the sensing and actuation.

procedure by assigning a different far-field (or outflow) boundary condition such as $u_r|_{r=R_\infty}^{n+1} = \cos\theta + \phi R/R_\infty$ (Choi 1998).

4.2. *Formulation of actuation*

After finding the Fréchet differential states, we obtain the actuation value ϕ of minimizing or maximizing the cost functional J by the use of a gradient algorithm,

$$\phi^{n+1^{l+1}} - \phi^{n+1^{l}} = \varrho \frac{\mathscr{D}J\left(\phi^{n+1^{l}}\right)}{\mathscr{D}\phi^{n+1}}, \tag{4.23}$$

where the superscript l denotes the iteration index, and ϱ is the descent/ascent parameter which is negative for minimization and positive for maximization. Then the cost functional J is minimized or maximized by (4.23) as follows:

$$J\left(\phi^{n+1^{l+1}}\right) \approx J\left(\phi^{n+1^{l}}\right) + \frac{\mathscr{D}J\left(\phi^{n+1^{l}}\right)}{\mathscr{D}\phi^{n+1}}\left(\phi^{n+1^{l+1}} - \phi^{n+1^{l}}\right), \tag{4.24}$$

$$J\left(\phi^{n+1^{l+1}}\right) \approx J\left(\phi^{n+1^{l}}\right) + \varrho\left|\frac{\mathscr{D}J\left(\phi^{n+1^{l}}\right)}{\mathscr{D}\phi^{n+1}}\right|^2. \tag{4.25}$$

In this section, we restrict the sensing and actuation to local regions of the cylinder surface. That is, the actuation ϕ is applied to a region of $\alpha \leqslant \theta \leqslant \beta$ and the sensing is restricted to a region of $\gamma \leqslant \theta \leqslant \delta$ (see, for example, figure 3).

4.2.1. *Cost functional* J_1

As mentioned in § 3, the cost functional J_1 is the pressure drag of a circular cylinder. Let us rewrite (3.1) in the more convenient mathematical form

$$J_1(\phi_1) = \int_0^{2\pi} P_1 R \,\mathrm{d}\theta, \tag{4.26}$$

where

$$P_1 = \begin{cases} -p|_{r=R}\cos\theta & \text{for } \gamma \leqslant \theta \leqslant \delta \\ 0 & \text{otherwise.} \end{cases} \tag{4.27}$$

Taking the Fréchet derivative of (4.26) and (4.27) with the use of (4.2) yields

$$\frac{\mathscr{D}J_1(\phi_1)}{\mathscr{D}\phi_1}\tilde{\phi}_1 = \int_0^{2\pi} \frac{\mathscr{D}P_1}{\mathscr{D}\phi_1}\tilde{\phi}_1 R\,\mathrm{d}\theta \tag{4.28}$$

with

$$\frac{\mathscr{D}P_1}{\mathscr{D}\phi_1}\tilde{\phi}_1 = \begin{cases} -\rho|_{r=R}\cos\theta & \text{for } \gamma \leqslant \theta \leqslant \delta \\ 0 & \text{otherwise.} \end{cases} \tag{4.29}$$

From (4.16) and (4.19), we rearrange $\hat{\rho}|_{r=R}$ such that

$$\hat{\rho}(k)|_{r=R} = \hat{a}(k)\,\hat{\tilde{\phi}}_1(k) \tag{4.30}$$

with

$$\hat{a}(k) = \begin{cases} Y_0(=\text{constant}) & \text{for } k = 0 \\ \dfrac{2}{\Delta t_c}\dfrac{1}{|k|}Y_k & \text{for } k \neq 0, \end{cases} \tag{4.31}$$

$$Y_0 = \frac{\hat{\rho}_{r=R,k=0}}{\hat{\tilde{\phi}}_{1,k=0}}, \tag{4.32}$$

$$Y_k = \frac{A}{B}. \tag{4.33}$$

Now, we obtain $\rho(\theta)|_{r=R}$ from (4.30) using the convolution integral

$$\rho(\theta)|_{r=R} = \frac{1}{2\pi}\int_0^{2\pi} \big(a(\theta-\tau)\,\tilde{\phi}_1(\tau)\big)\mathrm{d}\tau. \tag{4.34}$$

From (4.29) and (4.34), (4.28) becomes

$$\begin{aligned} \frac{\mathscr{D}J_1(\phi_1)}{\mathscr{D}\phi_1}\tilde{\phi}_1 &= \int_\gamma^\delta \left\{-\frac{1}{2\pi}\int_0^{2\pi}\big(a(\theta-\tau)\,\tilde{\phi}_1(\tau)\big)\mathrm{d}\tau\cos\theta\right\}R\,\mathrm{d}\theta \\ &= \int_0^{2\pi}\left\{\frac{1}{2\pi}\int_\gamma^\delta -a(\tau-\theta)\cos\tau\,\mathrm{d}\tau\right\}\tilde{\phi}_1(\theta)R\,\mathrm{d}\theta. \end{aligned} \tag{4.35}$$

For an arbitrary $\tilde{\phi}_1$, we obtain the following equation:

$$\frac{\mathscr{D}J_1(\phi_1)}{\mathscr{D}\phi_1} = \frac{1}{2\pi}\int_\gamma^\delta -a(\tau-\theta)\cos\tau\,\mathrm{d}\tau. \tag{4.36}$$

Note that $\mathscr{D}J_1(\phi_1)/\mathscr{D}\phi_1$ is a function of θ only.

Then, the gradient algorithm (4.23), for minimization, becomes

$$\phi_1^{l+1}(\theta) - \phi_1^l(\theta) = \varrho\frac{\mathscr{D}J_1\left(\phi_1^l\right)}{\mathscr{D}\phi_1}, \tag{4.37}$$

where $\varrho < 0$. Note that in general one should iterate the procedure to obtain a converged blowing/suction value ϕ and minimum J. However, it is not practical to do iteration because time goes forward continuously in real situations. Therefore, only one iteration is allowed for practical implementation, which, of course, will not guarantee a minimum J. For the effect of the number of iterations, see Choi *et al.* (1993*b*).

Since we do not allow any iteration for practical implementation, the actuation

$\phi_1(\theta)$ of decreasing J_1 becomes

$$\phi_1(\theta) = \begin{cases} -\dfrac{\varrho}{2\pi}\displaystyle\int_\gamma^\delta a(\tau-\theta)\cos\tau\,\mathrm{d}\tau & \text{for } \alpha \leqslant \theta \leqslant \beta \\ 0 & \text{otherwise.} \end{cases} \tag{4.38}$$

Here the actuation ϕ_1 is applied to the region $\alpha \leqslant \theta \leqslant \beta$. Note that the convolution integral in (4.38) does not include any flow variables in time and is a function of θ only. The actuation ϕ_1, therefore, does not require any flow information such as the wall pressure (i.e. no sensing is required) and is steady in time.

When we require the sensing and actuation to take place all over the cylinder surface (i.e. $(\gamma, \delta) = (0, 2\pi)$ and $(\alpha, \beta) = (0, 2\pi)$), $\phi_1(\theta)$ becomes (for the details, see Appendix B)

$$\phi_1(\theta) = -\varrho\frac{2}{\Delta t_c} Y_1 \cos\theta, \tag{4.39}$$

with

$$Y_1 = \frac{RK_1(mR) - mR^2K_2(mR)}{2K_1(mR) - mRK_2(mR)}. \tag{4.40}$$

Note that Y_1 is constant and thus the actuation of decreasing J_1 with all surface sensing and actuation is a cosine function.

4.2.2. *Cost functional* J_2

As mentioned in § 3, the cost functional J_2 is the square of the difference between the target pressure (p_t) and the real pressure (p) on the cylinder surface. Let us rewrite (3.2) as was done in § 4.2.1:

$$J_2(\phi_2) = \frac{1}{2}\int_0^{2\pi} P_2^2 R\,\mathrm{d}\theta, \tag{4.41}$$

where

$$P_2 = \begin{cases} p_t - p|_{r=R} & \text{for } \gamma \leqslant \theta \leqslant \delta \\ 0 & \text{otherwise.} \end{cases} \tag{4.42}$$

The actuation value $\phi_2(\theta)$ of decreasing J_2 can be easily obtained by following the same procedure in § 4.2.1. The blowing/suction value $\phi_2(\theta)$ of decreasing J_2 is

$$\phi_2(\theta) = \begin{cases} -\dfrac{\varrho}{2\pi}\displaystyle\int_0^{2\pi} P_2(\tau) a(\tau-\theta)\,\mathrm{d}\tau & \text{for } \alpha \leqslant \theta \leqslant \beta \\ 0 & \text{otherwise,} \end{cases} \tag{4.43}$$

where $\varrho < 0$. Note that the convolution integral in (4.43) requires pressure information on the cylinder surface for $\gamma \leqslant \theta \leqslant \delta$. Therefore, sensing of the instantaneous wall pressure on $\gamma \leqslant \theta \leqslant \delta$ is necessary to determine the actuation ϕ_2 on $\alpha \leqslant \theta \leqslant \beta$.

4.2.3. *Cost functional* J_3

As mentioned in § 3, the cost functional J_3 is the square of the pressure gradient on the cylinder surface. Let us rewrite (3.3) as was done in § 4.2.1:

$$J_3(\phi_3) = \frac{1}{2}\int_0^{2\pi} P_3^2 R\,\mathrm{d}\theta, \tag{4.44}$$

where

$$P_3 = \begin{cases} \partial p/\partial\theta|_{r=R} & \text{for } \gamma \leqslant \theta \leqslant \delta \\ 0 & \text{otherwise.} \end{cases} \tag{4.45}$$

The actuation value $\phi_3(\theta)$ of increasing J_3 can be obtained by following the same procedure as in § 4.2.1. The blowing/suction value $\phi_3(\theta)$ of increasing J_3 is

$$\phi_3(\theta) = \begin{cases} \dfrac{\varrho}{2\pi}\displaystyle\int_0^{2\pi} P_3(\tau) b\,(\tau-\theta)\mathrm{d}\tau & \text{for } \alpha \leqslant \theta \leqslant \beta \\ 0 & \text{otherwise,} \end{cases} \tag{4.46}$$

where $\varrho > 0$ and the Fourier coefficient of $b(\theta)$ is

$$\hat{b}\,(k) = \mathrm{i}k\hat{a}(k) = \begin{cases} 0 & \text{for } k = 0 \\ \dfrac{2}{\Delta t_c}\dfrac{\mathrm{i}k}{|k|}Y_k & \text{for } k \neq 0. \end{cases} \tag{4.47}$$

Note that sensing of the instantaneous wall pressure gradient on $\gamma \leqslant \theta \leqslant \delta$ is required to determine the actuation ϕ_3 on $\alpha \leqslant \theta \leqslant \beta$.

In the present study, we fix the maximum value of $|\phi(\theta)|$ (maximum blowing or suction speed relative to the free-stream velocity), $\phi_{max} = \max_{0\leqslant\theta<2\pi}|\phi(\theta)|$, and change ϱ at every control time step to satisfy this constraint.

As is shown in this section, our approach bypasses the adjoint problem and directly solves the Fréchet differential equations using the Fourier transformation. In order to obtain the control input ϕ, one has to know the Fréchet derivative of the cost functional $\mathscr{D}J/\mathscr{D}\phi$ (see (4.23)) which is usually a function of the Fréchet differential states (q_i, ρ). With the adjoint approach, $\mathscr{D}J/\mathscr{D}\phi$ is obtained by solving the linearized adjoint Navier–Stokes equations with appropriate adjoint boundary conditions which are closely associated with the definition of the cost functional (see Choi *et al.* 1993*b*). Thus, one has to solve the linearized adjoint Navier–Stokes equations whenever the cost functional is newly defined. With the present approach, however, the Fréchet differential states (q_i, ρ) are directly obtained from the Fréchet differential equations and thus knowledge of the cost functional is not required to determine q_i and ρ (as shown in § 4.1). Once q_i and ρ are obtained, $\mathscr{D}J/\mathscr{D}\phi$ can be easily determined (as shown in § 4.2). The disadvantage of the present method is that this approach is limited to very simple flow geometry problems such as channels or cylinders. Complex geometry problems such as flow over a backward-facing step cannot be solved by the present approach because of the Fourier transformation procedure and should be solved by the adjoint approach. Thus, the adjoint approach is a general tool for optimization problems. For the optimization problem investigated in this paper, these two approaches produce the same control input ϕ.

5. Results

As was mentioned in § 4, the pressures on the cylinder surface are measured at $\gamma \leqslant \theta \leqslant \delta$ and the blowing and suction are applied at $\alpha \leqslant \theta \leqslant \beta$. In § 5.1, sensings and actuations are carried out all over the cylinder surface, i.e. $(\alpha, \beta) = (\gamma, \delta) = (0, 2\pi)$. Local sensings and actuations are performed in § 5.2. Finally, open-loop controls are investigated in § 5.3.

For all cases investigated in this study, we have used the computational time step $\Delta t = 0.015$, and the control time interval $\Delta t_c = 0.06$. That is, the sensing and actuation are updated at every four computational time steps. We have also

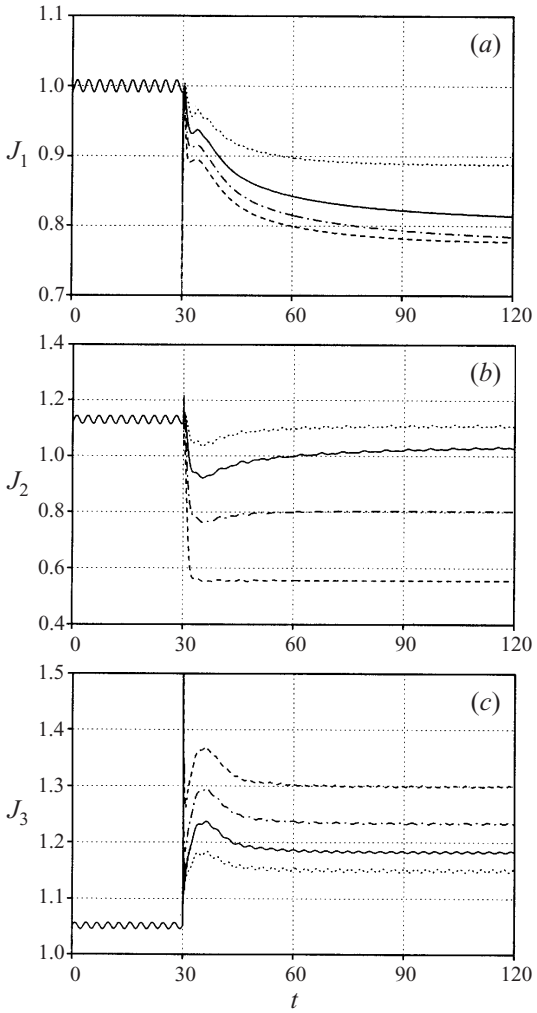

FIGURE 4. Time histories of the cost functional with $(\alpha, \beta) = (\gamma, \delta) = (0, 2\pi)$: ·····, $\phi_{max} = 0.1$; ——, 0.2; —·—·—, 0.3; – – – –, 0.4. (*a*) J_1; (*b*) J_2; (*c*) J_3.

investigated a few different combinations of Δt and Δt_c, but the results showed only a slight change compared to those obtained from $\Delta t = 0.015$ and $\Delta t_c = 0.06$. The Reynolds numbers investigated in this study (two-dimensional computations) are 100 and 160; according to the recent result by Henderson (1997), the two-dimensional wake becomes absolutely unstable to long-wavelength spanwise perturbations and bifurcates to a three-dimensional flow at $Re \approx 190$ (mode A; see also Williamson 1988). All controls begin at $t = 30$ and the maximum blowing/suction value relative to the free-stream velocity, $\phi_{max} = \max_{0 \leqslant \theta < 2\pi} |\phi(\theta)|$, is kept constant during the control.

5.1. *Sensing and actuation all over the cylinder surface*

We have applied the actuation values of decreasing J_1 and J_2 and of increasing J_3, respectively, to the flow of a circular cylinder at $Re = 100$. The target pressure in J_2 is taken to be the inviscid flow pressure, $p_t = p_\infty + \frac{1}{2}\rho u_\infty^2 (1 - 4\sin^2\theta)$ (see figure 2).

Figure 4 shows the time histories of the cost functional with blowing/suction. As

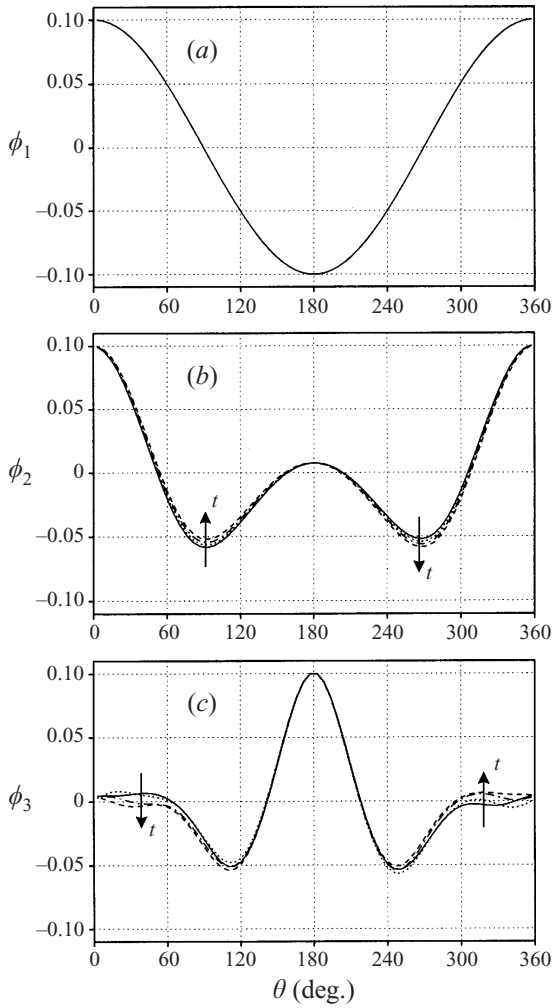

FIGURE 5. Actuation profiles: (*a*) $\phi_{1,max} = 0.1$; (*b*) $\phi_{2,max} = 0.1$; (*c*) $\phi_{3,max} = 0.1$. Here, $\theta = 180°$ corresponds to the stagnation point.

the controls are applied at $t \geqslant 30$, J_1 and J_2 decrease and J_3 increases at a given ϕ_{max} compared to the case of no control ($t < 30$). Also from figure 4, with increasing ϕ_{max} J_1 and J_2 further decrease and J_3 increases. Abrupt changes of J near $t = 30$ are due to the abrupt starting of the control. As will be shown later, vortex shedding completely disappears at large ϕ_{max}.

Figure 5 shows profiles of blowing/suction approximately for a half-cycle of vortex shedding (in figure 4, $112.2 \leqslant t \leqslant 115.2$ for J_1 and J_2, $113.4 \leqslant t \leqslant 116.4$ for J_3, respectively) in the case of $\phi_{max} = 0.1$. Note that ϕ_1 does not change in time, whereas ϕ_2 and ϕ_3 change periodically in time. The unsteadiness of the actuations disappears when $\phi_{2,max}$ and $\phi_{3,max}$ are sufficiently large to make the flow steady (no vortex shedding). It is interesting to note that the profiles of blowing/suction are very different among three cost functionals. That is, for ϕ_1 blowing is applied to the rear part and suction is to the front part of the cylinder surface. For ϕ_2, blowing is applied to the rear part and suction is to the upper and lower parts of the cylinder surface.

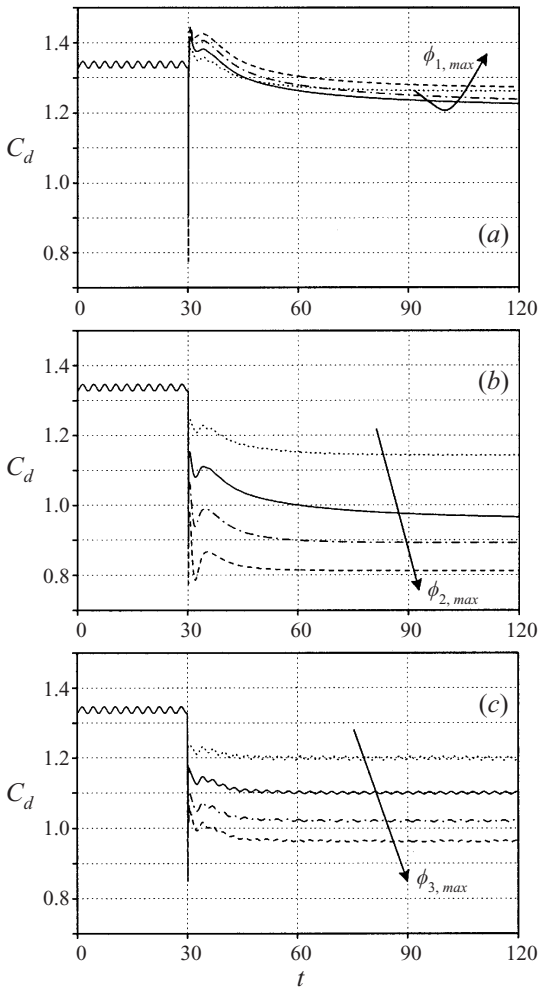

FIGURE 6. Time histories of the drag coefficient with $(\alpha, \beta) = (\gamma, \delta) = (0, 2\pi)$: ·····, $\phi_{max} = 0.1$; ——, 0.2; —·—·—, 0.3; – – – –, 0.4. (*a*) J_1; (*b*) J_2; (*c*) J_3.

For ϕ_3, blowing is applied to the front part and suction is to the upper and lower parts of the cylinder surface. As we will see later, all of these blowing/suction profiles successfully control vortex shedding and thus reduce drag.

Figures 6 and 7 show the time histories of the drag and lift coefficients with blowing/suction, respectively. For all actuations, the total drag of the cylinder is significantly reduced and the lift fluctuation of the cylinder is also reduced successfully. As anticipated in § 3, decreasing J_1 and J_2 and increasing J_3 result in drag reduction. It is interesting to note the variation of C_d with varying ϕ_{max} in figure 6. In the cases of J_2 and J_3, the C_d decrease further with increasing ϕ_{max}. The same trend of C_d variation, however, does not appear in the case of J_1, i.e. C_d first decreases and then increases as $\phi_{1,max}$ increases (at $t = 120$, $C_d = 1.26$, 1.21, 1.23 and 1.27 for $\phi_{1,max} =$ 0.1, 0.2, 0.3 and 0.4, respectively).

The different behaviours of C_d in cases J_1, J_2 and J_3 can be easily explained by examining the components of total drag. Figures 8(*a*), 8(*b*) and 8(*c*) show the time histories of the pressure drag and skin-friction drag coefficients with blowing/suction

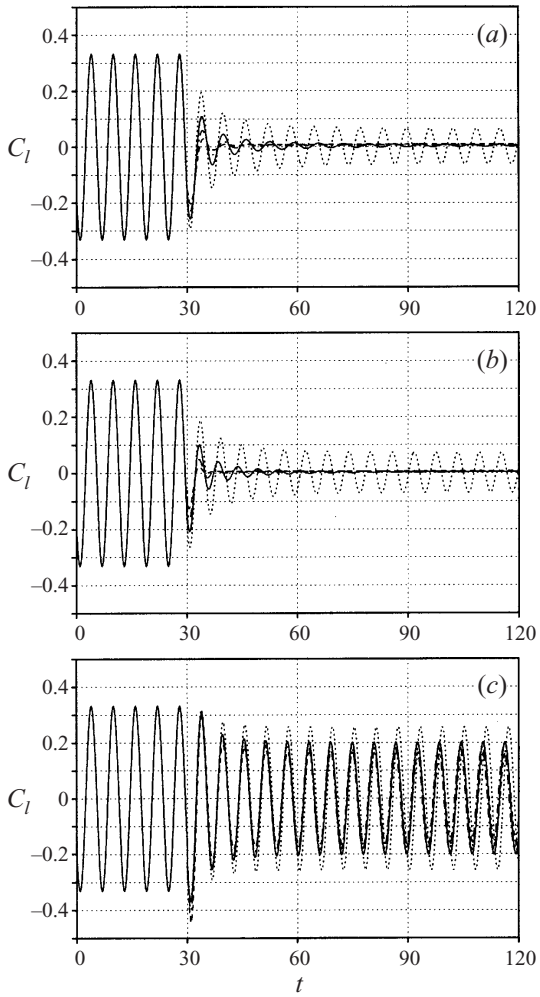

FIGURE 7. Time histories of the lift coefficient with $(\alpha, \beta) = (\gamma, \delta) = (0, 2\pi)$: ·····, $\phi_{max} = 0.1$; ———, 0.2; —·—·—, 0.3; – – – –, 0.4. (*a*) J_1; (*b*) J_2; (*c*) J_3.

in the cases of J_1, J_2 and J_3, respectively. As ϕ_{max} increases, C_{d_p} further decreases and C_{d_f} increases for J_1, J_2 and J_3. However, the amount of reduction in C_{d_p} in the case of J_1 is much smaller than those in the cases of J_2 and J_3. Since C_d is the sum of C_{d_p} and C_{d_f}, a decrease of C_{d_p} does not always guarantee a decrease of C_d. In order to reduce the pressure drag, one should increase the velocity gradient along the cylinder surface, which causes a separation delay. In this case, however, the skin-friction drag inevitably increases. Thus, inclusion of the skin-friction drag in the definition of J_1 does not always improve the result because decreasing the skin-friction drag increases the pressure drag.

Figure 9 shows the time-averaged velocity gradients along the cylinder surface with and without control. With control, the blowing and suction indeed increase the velocity gradient and thus delay the separation (see below), as ϕ_{max} increases. For the range of ϕ_{max} investigated in this study, the decrease of C_{d_p} is larger than the increase of C_{d_f} in the cases of J_2 and J_3, resulting in the monotonic decrease of total drag, whereas a non-monotonic behaviour is observed in the case of J_1 (figure 6). Note

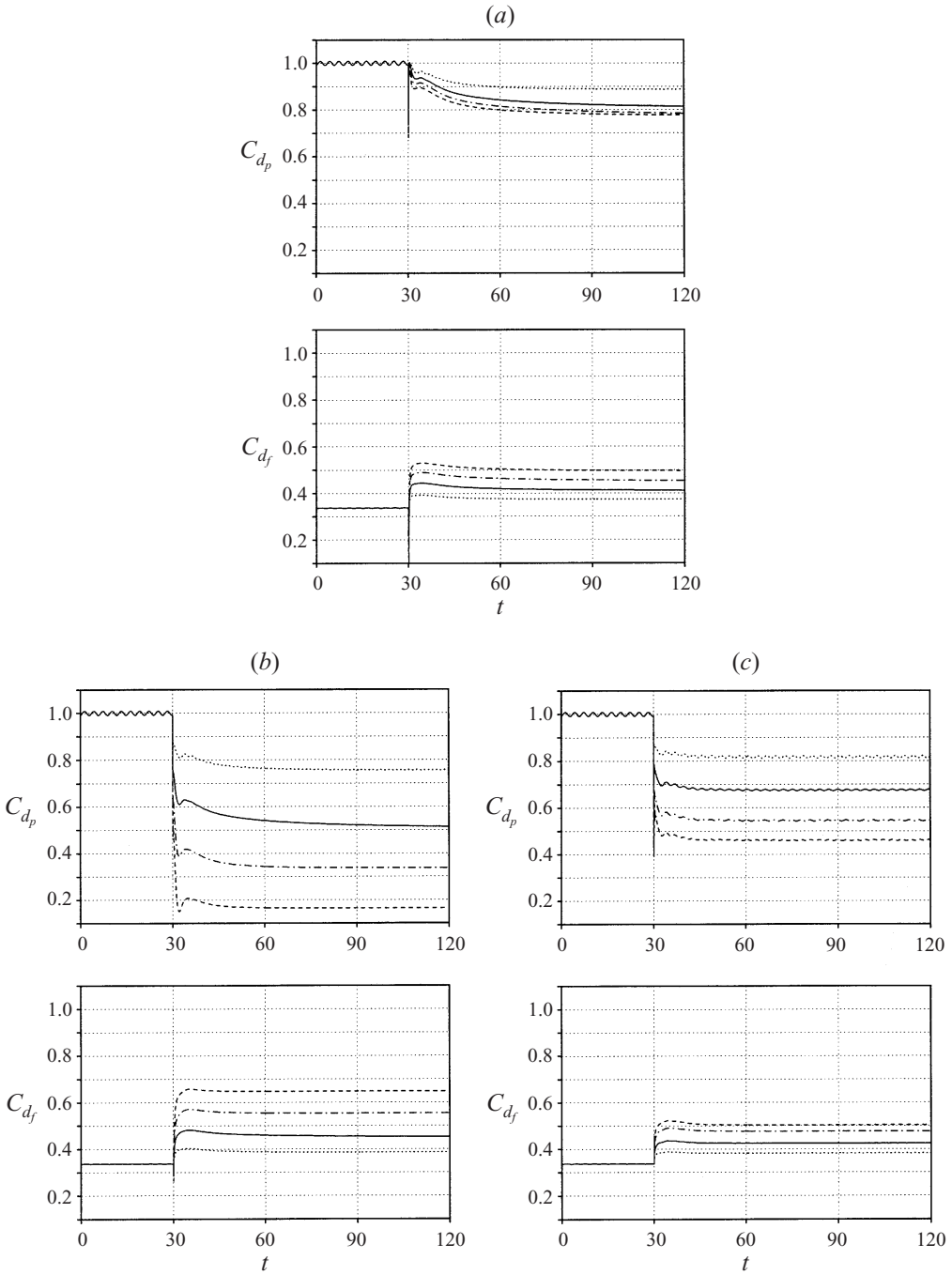

FIGURE 8. Time histories of the pressure drag coefficient (C_{d_p}) and skin-friction drag coefficient (C_{d_f}) with $(\alpha, \beta) = (\gamma, \delta) = (0, 2\pi)$: ·····, $\phi_{max} = 0.1$; ———, 0.2; —·—·—, 0.3; – – – –, 0.4. (*a*) J_1; (*b*) J_2; (*c*) J_3.

that, for all J, the C_l monotonically decrease due to attenuation of vortex shedding as ϕ_{max} increases (figure 7).

For a given ϕ_{max}, decreasing J_2 provides the largest drag reduction among the three

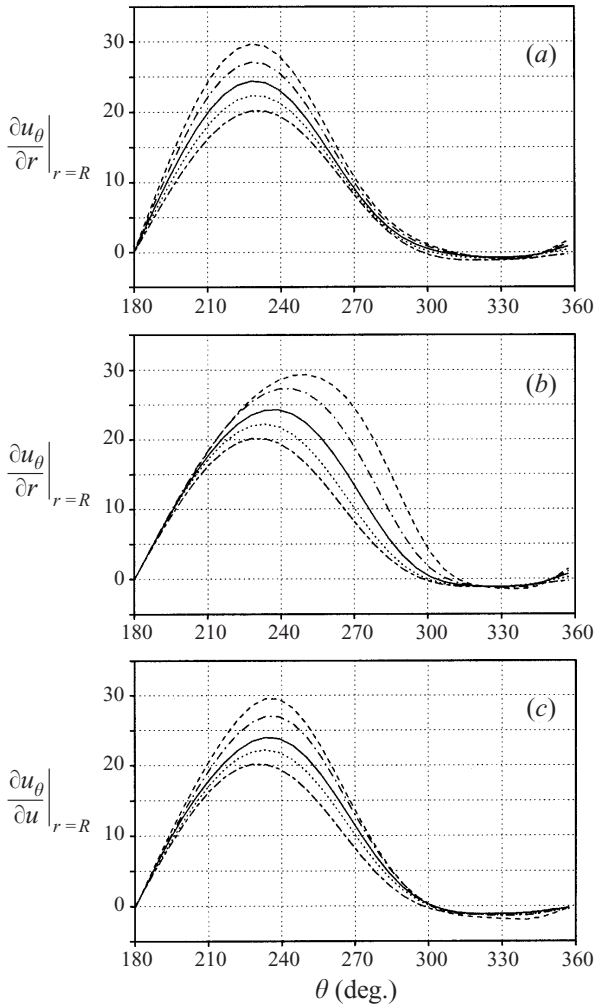

FIGURE 9. Time-averaged velocity gradients along the cylinder surface with $(\alpha, \beta) = (\gamma, \delta) = (0, 2\pi)$: ———, no control; ·····, $\phi_{max} = 0.1$; ———, 0.2; —·—·—, 0.3; – – – –, 0.4. (*a*) J_1; (*b*) J_2; (*c*) J_3.

cost functionals (figure 6). When $\phi_{max} = 0.2$, for example, about 9%, 28% and 17% drag reductions are obtained for J_1, J_2 and J_3, respectively. The efficiency of control is represented as the ratio of saved power to input power, $2(C_{d_0} - C_d)/\int_0^{2\pi}(|\phi|^3 + 2|p\phi|)\mathrm{d}\theta$, where C_{d_0} is the drag coefficient without control. The efficiencies are 0.6, 2.2 and 1.7 for J_1, J_2 and J_3, respectively.

It is interesting to note that the use of J_1 produced less pressure-drag reduction in comparison to J_2 and J_3, even though J_1 is directly related to the pressure drag. The cause of this may be two-fold. First, our control procedure looks for a local minimum or maximum of the cost functional. Because of the nonlinearity of the Navier–Stokes equations, the optimization problems of fluid flow are non-convex and thus the optimal control procedure does not guarantee the global minimum or maximum of the cost functional (Abergel & Temam 1990). In the present study, we used a gradient algorithm to look for the best control providing a local minimum or maximum of the cost functional (not a global one), and thus minimizing J_2 or

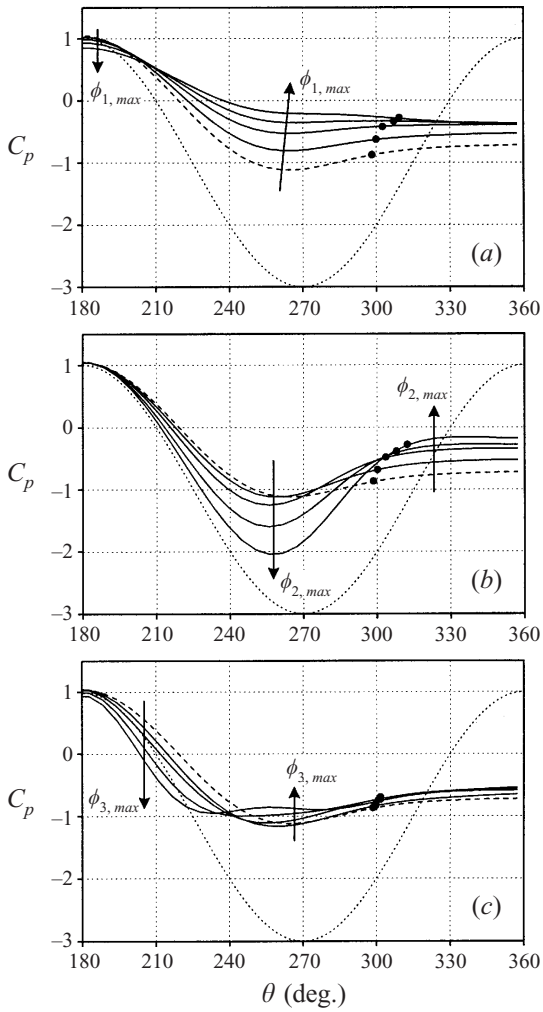

FIGURE 10. Time-averaged pressure coefficients with $(\alpha, \beta) = (\gamma, \delta) = (0, 2\pi)$: – – – –, no control; ·····, inviscid flow; ———, ϕ_{max} = 0.1, 0.2, 0.3 and 0.4. (*a*) J_1; (*b*) J_2; (*c*) J_3 (● denotes the separation point).

maximizing J_3 might produce a larger drag reduction than minimizing J_1. The second is that in this study we neglected the nonlinear terms in the Fréchet differential equations (4.10) for the practical implementation and thus inclusion of the nonlinear terms in (4.10) may change the drag-reduction performance. In that case, however, velocity information in the flow domain is required to determine the control input ϕ, which is clearly impractical in real situations.

Figure 10 shows the time-averaged pressure coefficients with blowing/suction. It can be seen that the C_p profiles of J_1, J_2 and J_3 are very different from one another. For J_1, C_p decreases near the stagnation point and increases at other surface locations as $\phi_{1,max}$ increases, which certainly decreases the pressure drag compared to no control. For J_2, C_p decreases near the front upper and lower parts and increases near the rear part as $\phi_{2,max}$ increases. Decrease of the pressure at the front part and significant increase of the base pressure lead to the largest reduction of the pressure drag among the three cost functionals (figure 8). Also it can be seen that, in the case of J_2, the

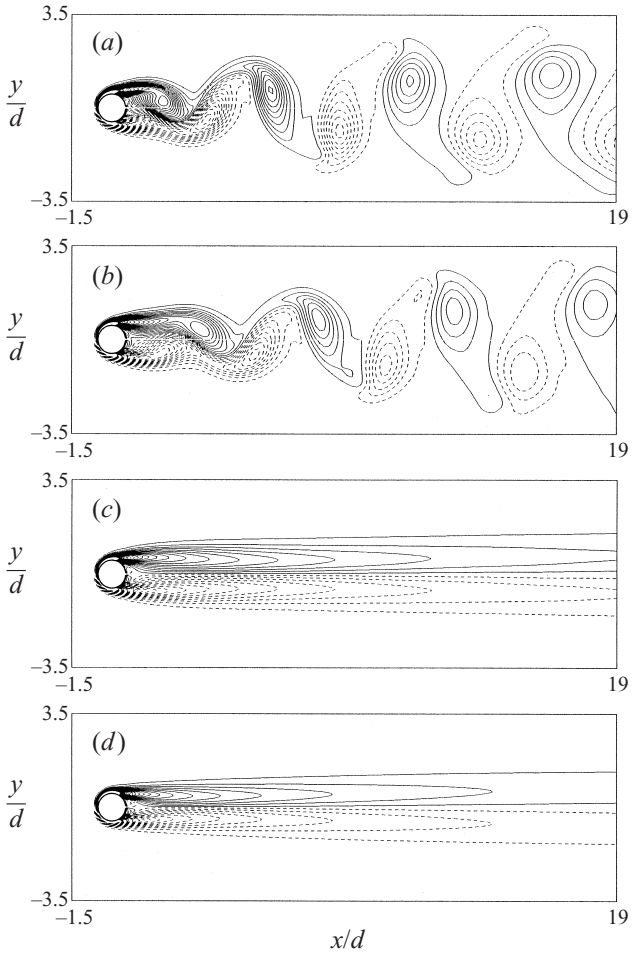

FIGURE 11. Instantaneous vorticity contours at $Re = 100$ with $(\alpha, \beta) = (\gamma, \delta) = (0, 2\pi)$: (*a*) no control; (*b*) $\phi_{2,max} = 0.1$; (*c*) 0.2; (*d*) 0.4. Contours are from −5.5 to 5.5 by increments of 0.2. Positive contours are dashed.

profile of C_p approaches that of the inviscid flow pressure coefficient with increasing $\phi_{2,max}$. Finally, for J_3, C_p significantly decreases near the front part of the cylinder as $\phi_{3,max}$ increases, whereas it shows a slight variation at the rear part as compared to no control. Thus, the pressure drag reduction is caused by the pressure decrease near the front part of the cylinder in the case of J_3. As is shown in figure 10, the separation point is delayed by control in all cases.

Figure 11 shows the instantaneous vorticity contours at $Re = 100$ with blowing/suction in the case of J_2. Vortex shedding behind the cylinder becomes weak at small $\phi_{2,max}$ and completely disappears at $\phi_{2,max} \geqslant 0.2$. For J_1 and J_3, not shown here, vortex shedding behind the cylinder also became weaker with increasing ϕ_{max}, and, at $0.3 \leqslant \phi_{max} \leqslant 0.4$, it completely disappeared for J_1 but still existed for J_3.

Roussopoulos (1993) and Park *et al.* (1994) reported that at low Reynolds numbers ($Re \leqslant 60$) their active control methods worked very well, resulting in no vortex shedding behind a circular cylinder. With increasing Reynolds number, however, vortex shedding behind the cylinder was not controlled very well. We, therefore, have

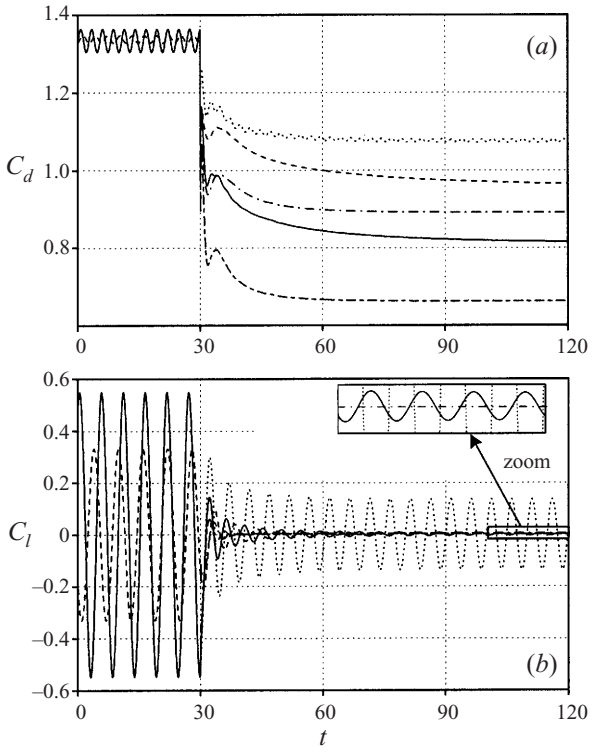

FIGURE 12. Time histories of the drag and lift coefficients with $(\alpha, \beta) = (\gamma, \delta) = (0, 2\pi)$: ·····, $Re = 160$ with $\phi_{2,max} = 0.1$; ———, $Re = 160$ with $\phi_{2,max} = 0.2$; — — —, $Re = 160$ with $\phi_{2,max} = 0.3$; – – – –, $Re = 100$ with $\phi_{2,max} = 0.2$; —·—·—, $Re = 100$ with $\phi_{2,max} = 0.3$. (*a*) C_d; (*b*) C_l.

simulated the flow at $Re = 160$ in the case of J_2 in order to see how a suboptimal feedback control method affects the flow at a different Reynolds number.

Figure 12 shows the time histories of the drag and lift coefficients with blowing/suction at $Re = 100$ and 160. When the Reynolds number increases from 100 to 160 in the case of no control, the drag/lift fluctuations significantly increase although the time-averaged mean drag coefficients are nearly the same (compare the solid line ($Re = 160$) with the dashed line ($Re = 100$) at $t < 30$ in figure 12). We can clearly see that the mean drag and the drag/lift fluctuations are successfully reduced by control at $Re = 160$. Moreover, the reductions of C_d at $Re = 160$ with $\phi_{2,max} = 0.2$ and 0.3 are larger than those at $Re = 100$ with $\phi_{2,max} = 0.2$ and 0.3. The efficiencies of control for these cases are 2.8 and 2.2 at $Re = 160$ with $\phi_{2,max} = 0.2$ and 0.3, and 2.2 and 1.5 at $Re = 100$ with $\phi_{2,max} = 0.2$ and 0.3, respectively. The efficiency, therefore, becomes better at a higher Reynolds number. On the other hand, figure 12(*b*) shows that lift fluctuations still exist at $Re = 160$ with $\phi_{2,max} = 0.1$ and 0.2 and disappear with $\phi_{2,max} = 0.3$, whereas there is no lift fluctuation at $Re = 100$ with $\phi_{2,max} = 0.2$ and 0.3, indicating that vortex shedding is more difficult to control at a higher Reynolds number (see also figure 13), which is the same conclusion as obtained by Roussopoulos (1993) and Park *et al.* (1994).

Figure 13 shows the instantaneous vorticity contours at $Re = 160$ with blowing/suction in the case of J_2. With $\phi_{2,max} = 0.2$, vortex shedding becomes significantly weak but still exists, resulting in the existence of lift fluctuations (figure 12*b*). With

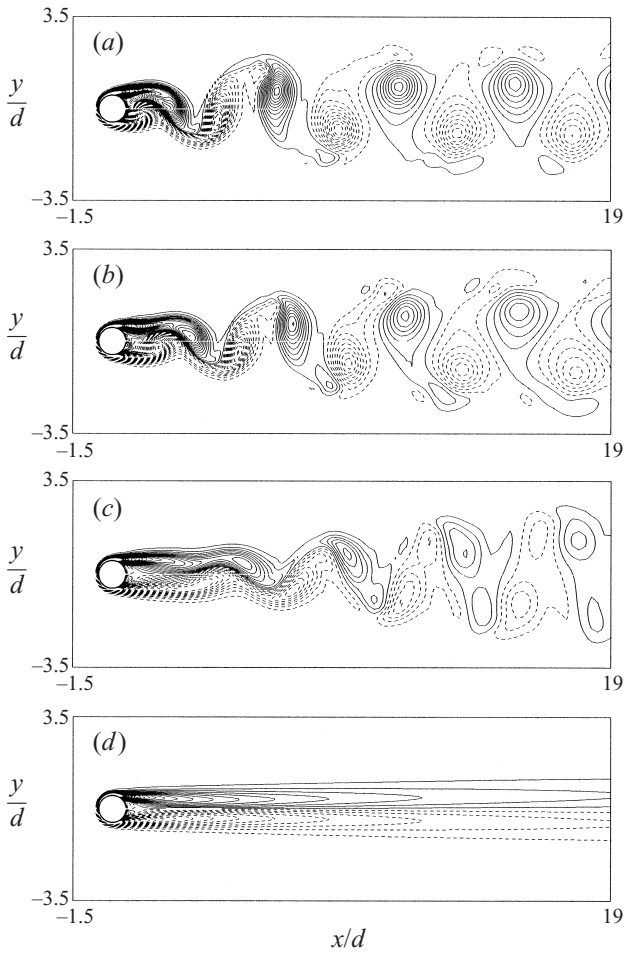

FIGURE 13. Instantaneous vorticity contours at $Re = 160$ with $(\alpha, \beta) = (\gamma, \delta) = (0, 2\pi)$: (*a*) no control; (*b*) $\phi_{2,max} = 0.1$; (*c*) 0.2; (*d*) 0.3. Contours are from −5.5 to 5.5 by increments of 0.2. Positive contours are dashed.

$\phi_{2,max} = 0.3$, however, vortex shedding completely disappears and there is no drag/lift fluctuation.

5.2. *Local sensing and actuation*

Results shown in § 5.1 are obtained from the sensing and actuation all over the cylinder surface. The formulation in § 4.2, however, is derived for sensing and actuation at arbitrary local areas on the cylinder surface. Also in view of practical implementation, local sensing and actuation are more useful. In this subsection, we show two examples of local sensing and actuation in the case of J_2 with $\phi_{2,max} = 0.2$.

Figure 14 shows a schematic of local sensing and actuation. The first case (case *A*) is sensing and actuation at the same areas, upper and lower parts of the cylinder surface: $(\alpha, \beta) = (\gamma, \delta) = (3\pi/8, \pi/2)$ and $(3\pi/2, 13\pi/8)$. The second case (case *B*) is sensing at the rear part and actuation at the upper and lower parts of the cylinder surface: $(\alpha, \beta) = (3\pi/8, \pi/2)$ and $(3\pi/2, 13\pi/8)$ and $(\gamma, \delta) = (-\pi/8, \pi/8)$. Note that the actuation areas of the two cases are the same.

Figure 15 shows the time histories of the drag and lift coefficients with local sensing

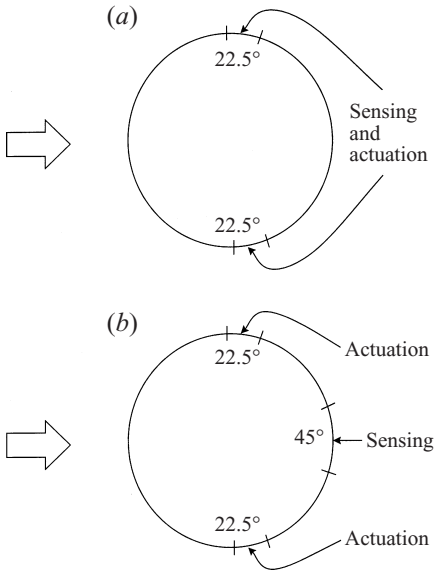

FIGURE 14. Schematic of local sensing and actuation: (*a*) case *A*; (*b*) case *B*.

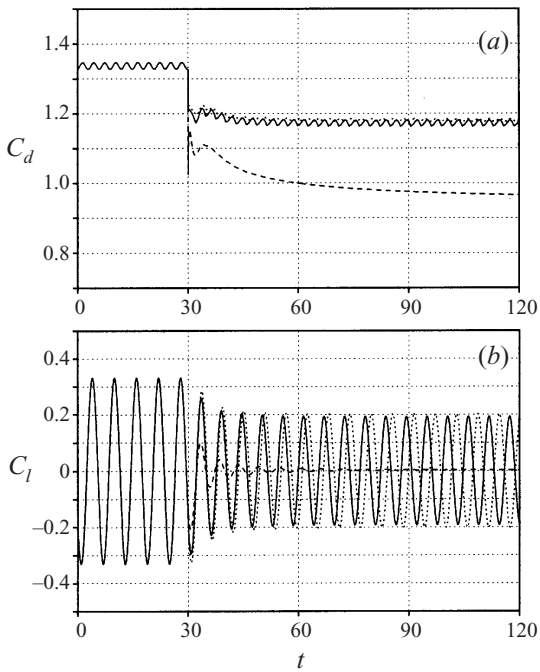

FIGURE 15. Time histories of the drag and lift coefficients at $Re = 100$ with $\phi_{2,max} = 0.2$: ———, case *A*; ·····, case *B*; – – – –, sensing/actuation all over the cylinder surface. (*a*) C_d; (*b*) C_l.

and actuation. In both cases, drag is reduced successfully. Drag reductions of cases *A* and *B* are about 12%, which is nearly half the drag reduction obtained from all surface sensing and actuation (28%). The efficiencies for cases *A* and *B* are 1.8 and 2.2, respectively. Considering that the sensing and actuation areas are reduced by a factor of 8, the amount of drag reduction from local sensing and actuation is quite

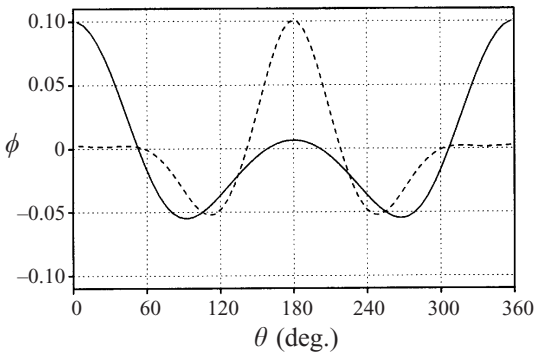

FIGURE 16. Time-averaged actuation profiles (open-loop control laws): ——, $\phi_{2,max} = 0.1$; – – – –, $\phi_{3,max} = 0.1$.

significant. In both cases A and B, the strength of vortices is reduced compared to no control.

5.3. *Open-loop control*

In general, feedback control is more efficient than non-feedback (or open-loop) control. However, feedback control requires instantaneous sensing of flow variables, which is quite difficult in practical situations. Therefore, one would like to obtain a simple open-loop control law without any flow sensing. In this section, simple and steady open-loop control laws of decreasing J_2 and increasing J_3 are obtained by averaging the unsteady actuations shown in figures 5(b) and 5(c) in time and applied to the flow behind a circular cylinder at $Re = 100$.

Figure 16 shows the time-averaged actuation profiles of decreasing J_2 and increasing J_3. Note that the time-averaged actuation profiles are slightly different from unsteady actuations (figure 5b, c). Figures 17 and 18 show the time histories of the cost functional and the drag and lift coefficients with open-loop controls, respectively, together with feedback controls. From figure 17, it is clear that open-loop controls also work well for decreasing J_2 and increasing J_3. The mean drag and drag/lift fluctuations are also significantly reduced with open-loop controls. The efficiencies of open-loop controls, therefore, are nearly the same as those of feedback controls. Moreover, it is interesting to note from figure 18 that for J_2, drag reduction is a little larger with open-loop control than with feedback control.

Results shown in this section are encouraging for the following reason. Once unsteady actuation profiles are obtained from a suboptimal feedback control for a bluff-body control problem, it is straightforward to obtain an open-loop actuation profile from them. Then a similarly successful result is expected from open-loop control which is much simpler and easier than feedback control.

6. Summary

The objective of this study was to develop a systematic method of controlling vortex shedding behind a bluff body using control theory. A suboptimal feedback control procedure for local sensing and local actuation was developed and applied to the flow behind a circular cylinder. The location of sensors for feedback was limited to the cylinder surface, and the control input from actuators was the blowing and suction on the cylinder surface. The three cost functionals to be minimized (J_1 and

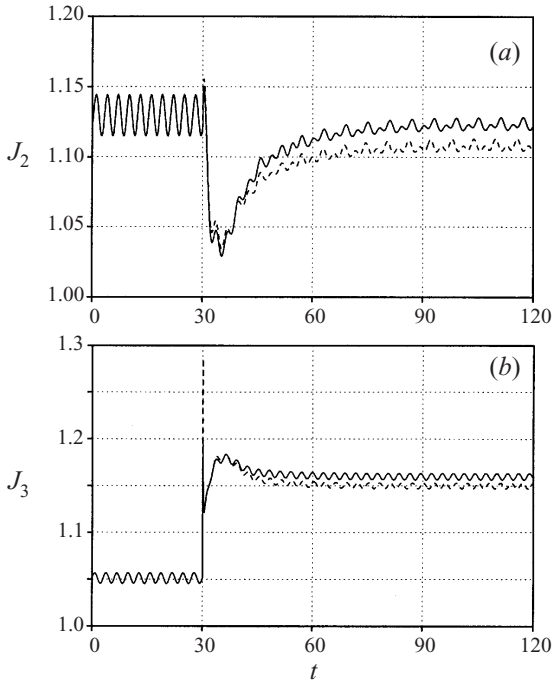

FIGURE 17. Time histories of the cost functional at $Re = 100$ with $(\alpha, \beta) = (\gamma, \delta) = (0, 2\pi)$ and $\phi_{max} = 0.1$: ———, open-loop control; – – – –, feedback control. (*a*) J_2; (*b*) J_3.

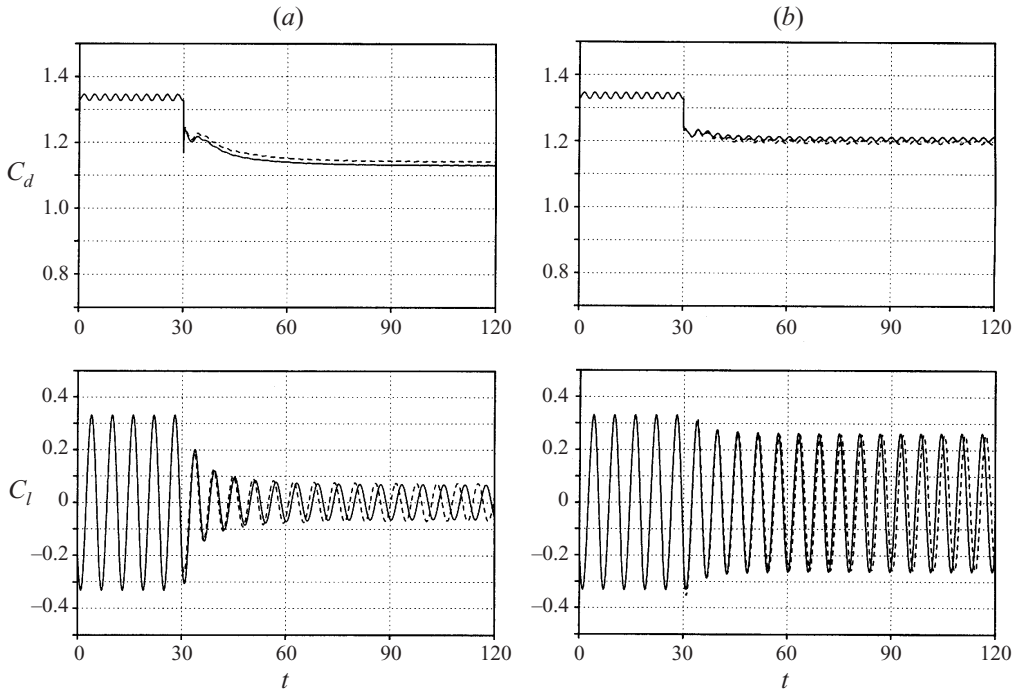

FIGURE 18. Time histories of the drag and lift coefficients at $Re = 100$ with $(\alpha, \beta) = (\gamma, \delta) = (0, 2\pi)$ and $\phi_{max} = 0.1$: ———, open-loop control; – – – –, feedback control. (*a*) J_2; (*b*) J_3.

J_2) or maximized (J_3) were the pressure drag of a cylinder (J_1), the square of the difference between the target pressure (inviscid flow pressure) and real flow pressure on the cylinder surface (J_2), and the square of the pressure gradient on the cylinder surface (J_3), respectively. Given the cost functionals, the flow variable to be measured by sensors and the control input from actuators were determined from the suboptimal feedback control procedure.

First, we applied blowing/suction to the flow of a circular cylinder at $Re = 100$. For all actuations, J_1 and J_2 successfully decreased and J_3 increased. Also, the mean drag and drag/lift fluctuations significantly decreased for all actuations. In the cases of J_2 and J_3, the C_d decreased further with increasing ϕ_{max}, whereas the same trend of the C_d variation did not appear in the case of J_1. For a given ϕ_{max}, reducing J_2 provided the largest drag reduction among the three cost functionals.

We also simulated the flow at $Re = 160$ in the case of J_2 in order to see how the control affected the flow at a different Reynolds number. The mean drag and drag/lift fluctuations were successfully decreased at $Re = 160$, and, moreover, the efficiency of reducing drag became better at a higher Reynolds number. However, it was also noted that vortex shedding was more difficult to control at a higher Reynolds number.

Two cases of local sensing and actuation were tested. One was with sensing and actuation at the same areas of the upper and lower parts of the cylinder surface and the other was with sensing at the rear part and actuation at the upper and lower parts of the cylinder surface. Both cases showed successful drag reduction and the strength of vortices was reduced by control.

By averaging the unsteady feedback actuations for J_2 and J_3 in time, simple and steady open-loop control laws were established, by which successful drag reduction was also achieved.

In two-dimensional laminar vortex shedding, flow patterns are periodic and predictable. Therefore, controlling vortex shedding at low Reynolds numbers is relatively easy. In turbulent flow, however, the flow becomes much more complex and is fully three-dimensional. A suboptimal feedback control of turbulent flow behind a circular cylinder is being investigated with actuation on a spanwise slot located at the upper and lower parts of the cylinder surface. The result will be reported in the future.

Financial supports from the academic research fund of the Korean Ministry of Education (ME97-B-02) and the Creative Research Initiatives of the Korean Ministry of Science and Technology are gratefully acknowledged.

Appendix A. Analytic solution of the Fréchet differential state equations

In a two-dimensional cylindrical coordinate, (4.10)–(4.13) become

$$q_r + \frac{\Delta t_c}{2}\frac{\partial \rho}{\partial r} - \frac{\Delta t_c}{2Re}\left(\frac{\partial^2 q_r}{\partial r^2} + \frac{1}{r}\frac{\partial q_r}{\partial r} + \frac{1}{r^2}\frac{\partial^2 q_r}{\partial \theta^2} - \frac{1}{r^2}q_r - \frac{2}{r^2}\frac{\partial q_\theta}{\partial \theta}\right) = 0, \tag{A 1}$$

$$q_\theta + \frac{\Delta t_c}{2}\frac{1}{r}\frac{\partial \rho}{\partial \theta} - \frac{\Delta t_c}{2Re}\left(\frac{\partial^2 q_\theta}{\partial r^2} + \frac{1}{r}\frac{\partial q_\theta}{\partial r} + \frac{1}{r^2}\frac{\partial^2 q_\theta}{\partial \theta^2} - \frac{1}{r^2}q_\theta + \frac{2}{r^2}\frac{\partial q_r}{\partial \theta}\right) = 0, \tag{A 2}$$

$$\frac{1}{r}q_r + \frac{\partial q_r}{\partial r} + \frac{1}{r}\frac{\partial q_\theta}{\partial \theta} = 0, \tag{A 3}$$

$$\frac{\partial^2 \rho}{\partial r^2} + \frac{1}{r}\frac{\partial \rho}{\partial r} + \frac{1}{r^2}\frac{\partial^2 \rho}{\partial \theta^2} = 0, \tag{A 4}$$

with

$$\left.\begin{aligned} q_r|_{r=R} &= \tilde{\phi}, \quad q_\theta|_{r=R} = 0, \\ q_r|_{r\to\infty} &= 0, \quad q_\theta|_{r\to\infty} = 0. \end{aligned}\right\} \tag{A 5}$$

The Fourier representations of (A 1)–(A 5) are

$$\hat{q}_r'' + \frac{1}{r}\hat{q}_r' - \left(\frac{2Re}{\Delta t_c} + \frac{k^2+1}{r^2}\right)\hat{q}_r - \frac{2ik}{r^2}\hat{q}_\theta - Re\hat{\rho}' = 0, \tag{A 6}$$

$$\hat{q}_\theta'' + \frac{1}{r}\hat{q}_\theta' - \left(\frac{2Re}{\Delta t_c} + \frac{k^2+1}{r^2}\right)\hat{q}_\theta + \frac{2ik}{r^2}\hat{q}_r - \frac{ik}{r}Re\hat{\rho} = 0, \tag{A 7}$$

$$\frac{1}{r}\hat{q}_r + \hat{q}_r' + \frac{ik}{r}\hat{q}_\theta = 0, \tag{A 8}$$

$$\hat{\rho}'' + \frac{1}{r}\hat{\rho}' - \frac{k^2}{r^2}\hat{\rho} = 0, \tag{A 9}$$

with

$$\left.\begin{aligned} &\hat{q}_r|_{r=R} = \hat{\tilde{\phi}}, \quad \hat{q}_\theta|_{r=R} = 0, \quad \hat{q}_r|_{r\to\infty} = 0, \quad \hat{q}_\theta|_{r\to\infty} = 0, \\ &q_r = \sum_k \hat{q}_r e^{ik\theta}, \quad q_\theta = \sum_k \hat{q}_\theta e^{ik\theta}, \\ &\rho = \sum_k \hat{\rho}\, e^{ik\theta}, \quad \tilde{\phi} = \sum_k \hat{\tilde{\phi}}\, e^{ik\theta}, \end{aligned}\right\} \tag{A 10}$$

where $\hat{q}_r$, $\hat{q}_\theta$, $\hat{\rho}$ and $\hat{\tilde{\phi}}$ are the Fourier coefficients of q_r, q_θ, ρ and $\tilde{\phi}$, respectively, k is the wavenumber in the θ-direction, and the prime denotes the differentiation with respect to the r-direction.

A.1. *Derivation of* (4.14)–(4.16)

When $k = 0$, (A 6)–(A 10) become

$$\hat{q}_r'' + \frac{1}{r}\hat{q}_r' - \left(\frac{2Re}{\Delta t_c} + \frac{1}{r^2}\right)\hat{q}_r - Re\,\hat{\rho}' = 0, \tag{A 11}$$

$$\hat{q}_\theta'' + \frac{1}{r}\hat{q}_\theta' - \left(\frac{2Re}{\Delta t_c} + \frac{1}{r^2}\right)\hat{q}_\theta = 0, \tag{A 12}$$

$$\frac{1}{r}\hat{q}_r + \hat{q}_r' = 0, \tag{A 13}$$

$$\hat{\rho}'' + \frac{1}{r}\hat{\rho}' = 0, \tag{A 14}$$

with

$$\left.\begin{aligned} &\hat{q}_r|_{r=R,k=0} = \hat{\tilde{\phi}}_{k=0}, \quad \hat{q}_\theta|_{r=R,k=0} = 0, \\ &\hat{q}_r|_{r\to\infty,k=0} = 0, \quad \hat{q}_\theta|_{r\to\infty,k=0} = 0. \end{aligned}\right\} \tag{A 15}$$

The general solution of (A 14) is

$$\hat{\rho}_{k=0} = X_1 + X_2 \ln r. \tag{A 16}$$

When $r \to \infty$, $\hat{\rho}$ should have a finite value, and thus $X_2 = 0$. Therefore, the solution of (A 14) is

$$\hat{\rho}_{k=0} = \hat{\rho}_{r=R,k=0}\,(= \text{constant}). \tag{A 17}$$

Differentiation of (A 17) gives

$$\hat{\rho}'_{k=0} = 0. \tag{A 18}$$

Substitution of (A 18) into (A 11) yields

$$\hat{q}''_r + \frac{1}{r}\hat{q}'_r - \left(\frac{2Re}{\Delta t_c} + \frac{1}{r^2}\right)\hat{q}_r = 0. \tag{A 19}$$

Note that (A 19) and (A 12) are modified Bessel equations, whose solutions are the composition of the modified Bessel functions (Hildebrand 1976):

$$\hat{q}_{r,k=0} = X_3 I_1(mr) + X_4 K_1(mr), \tag{A 20}$$

$$\hat{q}_{\theta,k=0} = X_5 I_1(mr) + X_6 K_1(mr), \tag{A 21}$$

where I_1 and K_1 are the modified Bessel functions of the first kind, of order 1, and the second kind, of order 1, respectively, and

$$m = \sqrt{\frac{2Re}{\Delta t_c}}. \tag{A 22}$$

From the boundary condition (A 15) we can determine the coefficients of (A 20) and (A 21), yielding

$$\hat{q}_{r,k=0} = \frac{\hat{\tilde{\phi}}_{k=0}}{K_1(mR)} K_1(mr), \tag{A 23}$$

$$\hat{q}_{\theta,k=0} = 0. \tag{A 24}$$

A.2. *Derivation of* (4.17)–(4.19)

When $k \neq 0$, (A 6)–(A 10) become

$$\hat{q}''_r + \frac{1}{r}\hat{q}'_r - \left(\frac{2Re}{\Delta t_c} + \frac{k^2+1}{r^2}\right)\hat{q}_r - \frac{2ik}{r^2}\hat{q}_\theta = Re\,\hat{\rho}', \tag{A 25}$$

$$\hat{q}''_\theta + \frac{1}{r}\hat{q}'_\theta - \left(\frac{2Re}{\Delta t_c} + \frac{k^2+1}{r^2}\right)\hat{q}_\theta + \frac{2ik}{r^2}\hat{q}_r = \frac{ik}{r}Re\,\hat{\rho}, \tag{A 26}$$

$$\frac{1}{r}\hat{q}_r + \hat{q}'_r + \frac{ik}{r}\hat{q}_\theta = 0, \tag{A 27}$$

$$\hat{\rho}'' + \frac{1}{r}\hat{\rho}' - \frac{k^2}{r^2}\hat{\rho} = 0, \tag{A 28}$$

with

$$\hat{q}_r|_{r=R,k\neq 0} = \hat{\tilde{\phi}}_{k\neq 0}, \tag{A 29}$$

$$\hat{q}_\theta|_{r=R,k\neq 0} = 0, \tag{A 30}$$

$$\hat{q}_r|_{r\to\infty,k\neq 0} = 0, \tag{A 31}$$

$$\hat{q}_\theta|_{r\to\infty,k\neq 0} = 0. \tag{A 32}$$

The general solution of (A 28) is

$$\hat{\rho} = X_7 r^k + X_8 r^{-k}. \tag{A 33}$$

When $r \to \infty$, $\hat{\rho}$ should have a finite value, and thus

$$X_8 = 0 \quad \text{for } k < 0 \quad \text{or} \quad X_7 = 0 \quad \text{for } k > 0. \tag{A 34a, b}$$

Therefore, the solution of (A 28) is

$$\hat{\rho}_{k\neq 0} = \hat{\rho}_{r=R,k\neq 0}\left(\frac{R}{r}\right)^{|k|} \tag{A 35}$$

with a new coefficient $\hat{\rho}_{r=R,k\neq 0}$, which will be determined later.

Differentiation of (A 35) gives

$$\hat{\rho}'_{k\neq 0} = -\frac{|k|}{r}\hat{\rho}_{r=R,k\neq 0}\left(\frac{R}{r}\right)^{|k|}. \tag{A 36}$$

Substitution of (A 36) and (A 35) into (A 25) and (A 26), respectively, yields

$$\hat{q}''_r + \frac{1}{r}\hat{q}'_r - \left(\frac{2Re}{\Delta t_c} + \frac{k^2+1}{r^2}\right)\hat{q}_r - \frac{2ik}{r^2}\hat{q}_\theta = -\frac{|k|}{r}Re\,\hat{\rho}_{r=R,k\neq 0}\left(\frac{R}{r}\right)^{|k|} \tag{A 37}$$

$$\hat{q}''_\theta + \frac{1}{r}\hat{q}'_\theta - \left(\frac{2Re}{\Delta t_c} + \frac{k^2+1}{r^2}\right)\hat{q}_\theta + \frac{2ik}{r^2}\hat{q}_r = \frac{ik}{r}Re\,\hat{\rho}_{r=R,k\neq 0}\left(\frac{R}{r}\right)^{|k|}. \tag{A 38}$$

Using (A 27), (A 37) becomes

$$\hat{q}''_r + \frac{3}{r}\hat{q}'_r - \left(\frac{2Re}{\Delta t_c} + \frac{k^2-1}{r^2}\right)\hat{q}_r = -\frac{|k|}{r}Re\,\hat{\rho}_{r=R,k\neq 0}\left(\frac{R}{r}\right)^{|k|}. \tag{A 39}$$

Note that when the right-hand side of (A 39) is zero, (A 39) is also a modified Bessel equation such as (A 12) or (A 19). Therefore, the homogeneous solution of (A 39) is

$$\hat{q}_{r_{ho}} = \frac{1}{r}\left\{X_8 I_{|k|}(mr) + X_9 K_{|k|}(mr)\right\}, \tag{A 40}$$

where $I_{|k|}$ and $K_{|k|}$ are the modified Bessel functions of the first kind, of order $|k|$, and the second kind, of order $|k|$, respectively.

Also the particular solution of (A 39) is obtained by assuming $\hat{q}_{r_{pa}} = X_{10}r^{\lambda}$,

$$\hat{q}_{r_{pa}} = \frac{\Delta t_c}{2}\frac{|k|}{r}\hat{\rho}_{r=R,k\neq 0}\left(\frac{R}{r}\right)^{|k|}. \tag{A 41}$$

From (A 40) and (A 41), the general solution of (A 39) is

$$\hat{q}_{r,k\neq 0} = X_8\frac{1}{r}I_{|k|}(mr) + X_9\frac{1}{r}K_{|k|}(mr) + \frac{\Delta t_c}{2}\frac{|k|}{r}\hat{\rho}_{r=R,k\neq 0}\left(\frac{R}{r}\right)^{|k|}. \tag{A 42}$$

From the boundary conditions (A 29) and (A 31) we can determine the coefficient of (A 42), yielding

$$\hat{q}_{r,k\neq 0} = \frac{\Delta t_c}{2}\frac{|k|}{r}\hat{\rho}_{r=R,k\neq 0}\left(\frac{R}{r}\right)^{|k|} + C\frac{1}{r}K_{|k|}(mr), \tag{A 43}$$

where

$$C = \frac{R\hat{\hat{\phi}}_{k\neq 0} - \frac{1}{2}\Delta t_c|k|\hat{\rho}_{r=R,k\neq 0}}{K_{|k|}(mR)}. \tag{A 44}$$

Differentiation of (A 43) gives

$$\hat{q}'_{r,k\neq 0} = -\frac{\Delta t_c}{2}\frac{|k|\left(|k|+1\right)}{r^2}\hat{\rho}_{r=R,k\neq 0}\left(\frac{R}{r}\right)^{|k|} + C\left\{-\frac{m}{r}K_{|k|+1}(mr) + \frac{|k|-1}{r^2}K_{|k|}(mr)\right\}, \tag{A 45}$$

where the differential relation between the modified Bessel functions K of orders n and $n+1$ is used,

$$\frac{\mathrm{d}}{\mathrm{d}r}K_n(mr) = -mK_{n+1}(mr) + \frac{n}{r}K_n(mr). \tag{A 46}$$

By substituting (A 43) and (A 45) into (A 27), we get the general solution of $\hat{q}_{\theta,k\neq 0}$,

$$\hat{q}_{\theta,k\neq 0} = \frac{\mathrm{i}}{k}\left\{-\frac{\Delta t_c}{2}\frac{|k|^2}{r}\hat{\rho}_{r=R,k\neq 0}\left(\frac{R}{r}\right)^{|k|} + \frac{|k|}{r}CK_{|k|}(mr) - mCK_{|k|+1}(mr)\right\}. \tag{A 47}$$

Note that (A 47) satisfies the boundary condition (A 32).

Now, let us determine the value $\hat{\rho}_{r=R,k\neq 0}$. From the boundary condition (A 30), we obtain

$$C\left\{\frac{|k|}{R}K_{|k|}(mR) - mK_{|k|+1}(mR)\right\} = \frac{\Delta t_c}{2}\frac{|k|^2}{R}\hat{\rho}_{r=R,k\neq 0}. \tag{A 48}$$

By substituting (A 44) into (A 48), we obtain the relation between $\hat{\rho}_{r=R,k\neq 0}$ and $\hat{\tilde{\phi}}_{k\neq 0}$ as follows:

$$\hat{\rho}_{r=R,k\neq 0} = \frac{2}{\Delta t_c}\frac{|k|K_{|k|}(mR) - mRK_{|k|+1}(mR)}{|k|\left\{(2|k|/R)K_{|k|}(mR) - mK_{|k|+1}(mR)\right\}}\hat{\tilde{\phi}}_{k\neq 0}. \tag{A 49}$$

From (A 44) and (A 49), we also get the relation between C and $\hat{\tilde{\phi}}_{k\neq 0}$,

$$C = \frac{R|k|}{2|k|K_{|k|}(mR) - mRK_{|k|+1}(mR)}\hat{\tilde{\phi}}_{k\neq 0}. \tag{A 50}$$

Substitution of (A 49) and (A 50) into (A 35), (A 43) and (A 47) yields

$$\hat{\rho}_{k\neq 0} = \frac{2}{\Delta t_c}\frac{1}{|k|}\hat{\tilde{\phi}}_{k\neq 0}\frac{A}{B}\left(\frac{R}{r}\right)^{|k|}, \tag{A 51}$$

$$\hat{q}_{r,k\neq 0} = \hat{\tilde{\phi}}_{k\neq 0}\frac{A\left(R/r\right)^{|k|} + R|k|K_{|k|}(mr)}{B\ r}, \tag{A 52}$$

$$\hat{q}_{\theta,k\neq 0} = \frac{\mathrm{i}|k|}{k}\hat{\tilde{\phi}}_{k\neq 0}\frac{-A\left(R/r\right)^{|k|} + \left\{R|k|K_{|k|}(mr) - mRrK_{|k|+1}(mr)\right\}}{B\ r}, \tag{A 53}$$

where

$$A = R|k|K_{|k|}(mR) - mR^2K_{|k|+1}(mR), \quad B = 2|k|K_{|k|}(mR) - mRK_{|k|+1}(mR). \tag{A 54}$$

Appendix B. Derivation of (4.39)

For $(\alpha,\beta) = (\gamma,\delta) = (0, 2\pi)$, (4.38) becomes

$$\phi_1(\theta) = -\frac{\varrho}{2\pi}\int_0^{2\pi} a(\tau-\theta)\cos\tau\,\mathrm{d}\tau. \tag{B 1}$$

Using (4.31)–(4.33) and the definition of the Fourier transformation

$$a(\theta) = \sum_k \hat{a}(k)\, \mathrm{e}^{\mathrm{i}k\theta}, \tag{B 2}$$

we obtain

$$a(\theta) = Y_0 + \frac{2}{\Delta t_c} \sum_{k \neq 0} \frac{Y_k}{|k|} \cos(k\theta). \tag{B 3}$$

From (B 3) one can easily get

$$a(\tau - \theta) = Y_0 + \frac{2}{\Delta t_c} \sum_{k \neq 0} \frac{Y_k}{|k|} \{\cos(k\tau)\cos(k\theta) + \sin(k\tau)\sin(k\theta)\}. \tag{B 4}$$

Substitution of (B 4) into (B 1) yields

$$\begin{aligned} \phi_1(\theta) = &-\frac{\varrho}{2\pi} \int_0^{2\pi} \{Y_0 \cos\tau\}\, \mathrm{d}\tau \\ &-\frac{\varrho}{2\pi} \int_0^{2\pi} \left\{ \frac{2}{\Delta t_c} \sum_{k \neq 0} \frac{Y_k}{|k|} \{\cos(k\tau)\cos(k\theta) + \sin(k\tau)\sin(k\theta)\} \cos\tau \right\} \mathrm{d}\tau. \end{aligned} \tag{B 5}$$

The first term of the right-hand side of (B 5) is identically zero. Application of the orthogonality of trigonometric functions to the second term of the right-hand side of (B 5) yields

$$\phi_1(\theta) = -\varrho \frac{2}{\Delta t_c} Y_1 \cos\theta \tag{B 6}$$

with

$$Y_1 = \frac{RK_1(mR) - mR^2 K_2(mR)}{2K_1(mR) - mRK_2(mR)}. \tag{B 7}$$

REFERENCES

Abergel, F. & Temam, R. 1990 On some control problems in fluid mechanics. *Theor. Comput. Fluid Dyn.* **1**, 303.

Apelt, C. J. & West, G. S. 1975 The effects of wake splitter plates on bluff-body flow in the range $10^4 < R < 5 \times 10^4$: Part 2. *J. Fluid Mech.* **71**, 145.

Apelt, C. J., West, G. S. & Szewczyk, A. A. 1973 The effects of wake splitter plates on the flow past a circular cylinder in the range $10^4 < R < 5 \times 10^4$. *J. Fluid Mech.* **61**, 187.

Bearman, P. W. 1967 The effect of base bleed on the flow behind a two-dimensional model with a blunt trailing edge. *Aero. Q.* **18**, 207.

Choi, H. 1998 Suboptimal feedback control of vortex shedding. *13th US National Congress of Applied Mechanics, Gainesville, Florida, June 1998.*

Choi, H., Moin, P. & Kim, J. 1992 Turbulent drag reduction: Studies of feedback control & flow over riblets. *Rep.* TF-55. Department of Mechanical Engineering, Stanford University, Stanford, CA.

Choi, H., Moin, P. & Kim, J. 1993*a* Direct numerical simulation of turbulent flow over riblets. *J. Fluid Mech.* **255**, 503.

Choi, H., Temam, R., Moin, P. & Kim, J. 1993*b* Feedback control for unsteady flow and its application to the stochastic Burgers equation. *J. Fluid Mech.* **253**, 509.

Cimbala, J. M. & Garg, S. 1991 Flow in the wake of a freely rotatable cylinder with splitter plate. *AIAA J.* **29**, 1001.

Finlayson, B. A. 1972 *The Method of Weighted Residuals and Variational Principles.* Academic.

Fornberg, B. 1980 A numerical study of steady viscous flow past a circular cylinder. *J. Fluid Mech.* **98**, 819.

GASTER, M. 1969 Vortex shedding from slender cones at low Reynolds numbers. *J. Fluid Mech.* **38**, 565.

GASTER, M. 1971 Vortex shedding from circular cylinders at low Reynolds numbers. *J. Fluid Mech.* **46**, 749.

GERICH, D. & ECKELMANN, H. 1982 Influence of end plates and free ends on the shedding frequency of circular cylinders. *J. Fluid Mech.* **122**, 109.

GERRARD, J. H. 1966 The mechanics of the formation region of vortices behind bluff bodies. *J. Fluid Mech.* **25**, 401.

GUNZBURGER, M. D., HOU, L. & SVOBONDY, T. P. 1990 A numerical method for drag minimization via the suction and injection of mass through the boundary. In *Stabilization of Flexible Structures* (ed. J. P. Zolesio). Springer.

GUNZBURGER, M. D., HOU, L. & SVOBONDY, T. P. 1991 Analysis and finite element approximations of optimal control problems for the stationary Navier–Stokes equations with Dirichlet controls. *Math. Model. Numer. Anal.* **25**, 711.

GUNZBURGER, M. D., HOU, L. & SVOBONDY, T. P. 1992 Boundary velocity control of incompressible flow with an application to viscous drag reduction. *SIAM J. Control Optim.* **30**, 167.

HENDERSON, R. D. 1995 Details of the drag curve near the onset of vortex shedding. *Phys. Fluids* **7**, 2102.

HENDERSON, R. D. 1997 Nonlinear dynamics and pattern formation in turbulent wake transition. *J. Fluid Mech.* **352**, 65–112.

HILDEBRAND, F. B. 1976 *Advanced Calculus for Applications*, 2nd Edn. Prentice-Hall.

KWON, K. & CHOI, H. 1996 Control of laminar vortex shedding behind a circular cylinder using splitter plates. *Phys. Fluids* **8**, 479.

LEE, C., KIM, J. & CHOI, H. 1998 Suboptimal control of turbulent channel flow for drag reduction. *J. Fluid Mech.* **358**, 245.

NISHIOKA, M. & SATO, H. 1974 Measurements of velocity distributions in the wake of a circular cylinder at low Reynolds numbers. *J. Fluid Mech.* **65**, 97.

OERTEL, H. 1990 Wakes behind blunt bodies. *Ann. Rev. Fluid Mech.* **22**, 539.

PANTON, R. L. 1996 *Incompressible Flow*, 2nd Edn. John Wiley & Sons.

PARK, D. S., LADD, D. M. & HENDRICKS, E. W. 1994 Feedback control of von Kármán vortex shedding behind a circular cylinder at low Reynolds numbers. *Phys. Fluids* **6**, 2390.

PAULEY, L. L., MOIN, P. & REYNOLDS, W. C. 1990 The structure of two-dimensional separation. *J. Fluid Mech.* **220**, 397.

ROSENFELD, M., KWAK, D. & VINOKUR, M. 1991 A fractional step solution method for the unsteady incompressible Navier–Stokes equations in generalized coordinate systems. *J. Comput. Phys.* **94**, 102.

ROSHKO, A. 1955 On the wake and drag of bluff bodies. *J. Aeronaut. Sci.* **22**, 124.

ROUSSOPOULOS, K. 1993 Feedback control of vortex shedding at low Reynolds numbers. *J. Fluid Mech.* **248**, 267.

SATAKE, S. & KASAGI, N. 1997 Suboptimal turbulence control with the body force of selective velocity damping localized to the near-wall region. *Proc. 11th Symp. Turbulent Shear Flows*, vol. 1, pp. P1.43–P1.48. Grenoble, September 1997.

SCHUMM, M., BERGER, E. & MONKEWITZ, P. A. 1994 Self-excited oscillations in the wake of two-dimensional bluff bodies and their control. *J. Fluid Mech.* **271**, 17.

SHAIR, F. H., GROVE, A. S., PETERSEN, E. E. & ACRIVOS, A. 1963 The effect of confining walls on the stability of the steady wake behind a circular cylinder. *J. Fluid Mech.* **17**, 547.

STANSBY, P. K. 1974 The effects of end plates on the base pressure coefficient of a circular cylinder. *Aerosp. J.* **78**, 36.

STRYKOWSKI, P. J. & SREENIVASAN, K. R. 1990 On the formation and suppression of vortex 'shedding' at low Reynolds numbers. *J. Fluid Mech.* **218**, 71.

TEMAM, R., BEWLEY, T. & MOIN, P. 1997 Control of turbulent flows. *Proc. 18th IFIP TC7 Conf. on System Modelling and Optimization, Detroit, Michigan, July 1997.*

THOMPSON, J. F., WARSI, Z. U. A. & MASTIN, C. W. 1985 *Numerical Grid Generation – Foundations and Application.* Elsevier.

TOKUMARU, P. T. & DIMOTAKIS, P. E. 1991 Rotary oscillatory control of a cylinder wake. *J. Fluid Mech.* **224**, 77.

TRITTON, D. J. 1987 *Physical Fluid Dynamics*, 2nd Edn. Oxford Science Publications.

Unal, M. F. & Rockwell, D. 1988 On vortex formation from a cylinder. Part 2. Control by splitter-plate interference. *J. Fluid Mech.* **190**, 513.

Williamson, C. H. K. 1988 The existence of two stages in the transition to three dimensionality of a cylinder wake. *Phys. Fluids* **31**, 3165.

Williamson, C. H. K. 1989 Oblique and parallel modes of vortex shedding in the wake of a circular cylinder at low Reynolds numbers. *J. Fluid Mech.* **206**, 579.

Williamson, C. H. K. 1996 Vortex dynamics in the cylinder wake. *Ann. Rev. Fluid Mech.* **28**, 477.

Wood, C. J. 1964 The effect of base bleed on a periodic wake. *J. R. Aeronaut. Soc.* **68**, 477.